van der Geest *et al.*
Acta Neuropathologica Communications (2024) 12:152
https://doi.org/10.1186/s40478-024-01857-1

Acta Neuropathologica Communications

RESEARCH

Open Access

Molecular pathology, developmental changes and synaptic dysfunction in (pre-) symptomatic human C9ORF72-ALS/FTD cerebral organoids

Astrid T. van der Geest[1], Channa E. Jakobs[1], Tijana Ljubikj[1], Christiaan F. M. Huffels[1], Marta Cañizares Luna[1], Renata Vieira de Sá[1], Youri Adolfs[1], Marina de Wit[1], Daan H. Rutten[1], Marthe Kaal[1], Maria M. Zwartkruis[2,4], Mireia Carcolé[3], Ewout J. N. Groen[2], Elly M. Hol[1], Onur Basak[1], Adrian M. Isaacs[3], Henk-Jan Westeneng[2], Leonard H. van den Berg[2], Jan H. Veldink[2], Domino K. Schlegel[1] and R. Jeroen Pasterkamp[1*]

Abstract

A hexanucleotide repeat expansion (HRE) in *C9ORF72* is the most common genetic cause of amyotrophic lateral sclerosis (ALS) and frontotemporal dementia (FTD). Human brain imaging and experimental studies indicate early changes in brain structure and connectivity in C9-ALS/FTD, even before symptom onset. Because these early disease phenotypes remain incompletely understood, we generated iPSC-derived cerebral organoid models from C9-ALS/FTD patients, presymptomatic *C9ORF72-HRE* (C9-HRE) carriers, and controls. Our work revealed the presence of all three C9-HRE-related molecular pathologies and developmental stage-dependent size phenotypes in cerebral organoids from C9-ALS/FTD patients. In addition, single-cell RNA sequencing identified changes in cell type abundance and distribution in C9-ALS/FTD organoids, including a reduction in the number of deep layer cortical neurons and the distribution of neural progenitors. Further, molecular and cellular analyses and patch-clamp electrophysiology detected various changes in synapse structure and function. Intriguingly, organoids from all presymptomatic C9-HRE carriers displayed C9-HRE molecular pathology, whereas the extent to which more downstream cellular defects, as found in C9-ALS/FTD models, were detected varied for the different presymptomatic C9-HRE cases. Together, these results unveil early changes in 3D human brain tissue organization and synaptic connectivity in C9-ALS/FTD that likely constitute initial pathologies crucial for understanding disease onset and the design of therapeutic strategies.

Keywords ALS, Brain, Neural organoid, C9ORF72, Development, Presymptomatic

*Correspondence:
R. Jeroen Pasterkamp
r.j.pasterkamp@umcutrecht.nl
Full list of author information is available at the end of the article

Introduction

Amyotrophic lateral sclerosis (ALS) is a fatal adult-onset neurodegenerative disease characterized by the progressive loss of lower and upper motor neurons resulting in muscle weakness and atrophy [33]. Median survival is 3–5 years after symptom onset and treatment options are limited for ALS patients. More effective therapies are needed, but their development requires a better understanding of the pathogenic mechanisms underlying ALS. The disease has a strong genetic contribution and an intronic hexanucleotide repeat expansion (HRE) in *C9ORF72* is the most common genetic cause of ALS. *C9ORF72-HREs* (C9-HRE) are also a frequent cause of frontotemporal dementia (FTD) and occur in patients that suffer from both ALS and FTD [29, 92]. Mechanistically, C9-HRE results in C9ORF72 haploinsufficiency, formation of RNA foci and dipeptide repeat proteins (DPRs), and TDP-43 pathology [7, 111, 112] leading to incompletely understood downstream molecular and cellular defects.

Although the pathogenic effects of C9-HRE on spinal motor neurons are studied intensely, how other types of neurons, e.g. in the motor or frontal cortex, are affected is less well understood. This is in part due to the paucity of protocols for generating human cortical motor neurons and the lack of mouse models that faithfully recapitulate C9-HRE pathogenesis. However, multiple observations indicate prominent changes in the cortex and other brain regions in C9-ALS/FTD. These include human imaging studies showing for example cortical thinning, altered connectivity and cortical hyperexcitability, even at early presymptomatic stages [13, 16, 41, 63, 64, 76, 77, 113, 120]. Further, transcriptomic and proteomic analyses of human post-mortem brain tissue identify specific molecular changes, including in vulnerable cell types such as deep layer cortical neurons (e.g. [17, 45, 66, 86, 100, 109]). Thus, while changes in brain structure and connectivity are a hallmark of C9-ALS/FTD, our understanding of the molecular and cellular deficits that lead to these phenotypes in humans is rather rudimentary.

ALS patients usually develop symptoms between 51 and 66 years of age [67], but accumulating evidence supports the idea that ALS, and other adult-onset neurodegenerative diseases such as for example Huntington's disease [5, 8], are caused by a sequence of pathogenic events some of which may have a developmental origin and occur far in advance of the onset of first symptoms. For example, the toxic products of C9-HRE can be detected at early presymptomatic stages in ALS/FTD and impair neurogenesis at embryonic stages in human stem cell cultures and in vivo in mice [48, 88, 111]. In addition, multiple human imaging studies report structural changes in the brain of C9-HRE carriers, such as cortical thinning and altered gyrification, decades before the average age of disease onset [11, 13, 18, 35, 64, 93, 113]. The slope of decline with age of these structural changes, e.g. cortical thickness, is similar for C9-HRE carriers and non-carriers, supporting an early, perhaps developmental, origin of the initial pathogenic events [64, 113]. This is in line with C9ORF72 expression patterns at embryonic and postnatal stages [6, 34, 65]. Although these observations hint at early, developmental effects of C9-HRE leading to detrimental structural and connectivity changes in the adult, the cellular defects that underlie these phenotypes in the complex environment of human brain tissue remain largely unknown.

Here, we generate and use unguided neural organoid models (referred to as cerebral organoids [60]) derived from induced pluripotent stem cells (iPSCs) of C9-ALS/FTD patients and healthy controls to study changes in cellular architecture and connectivity. The resemblance of cerebral organoids to the three-dimensional character and composition of human brain tissue provides a unique opportunity to investigate the spatiotemporal mechanisms that dictate human brain development and disease [3, 23, 61, 84, 110, 114, 116]. We combined single-cell RNA sequencing, molecular and cellular approaches, and patch-clamp electrophysiology to detect all three C9-HRE pathological hallmarks and developmental changes in growth, cellular composition, and synapses. Specifically, a reduction in the number of deep layer neurons was found concomitant with molecular, structural, and functional changes in excitatory synapses.

Previous work shows that presymptomatic C9-HRE carriers display several (e.g. altered brain structure, cryptic exon inclusion) but not all (e.g. elevated serum Nf-L) of the phenotypes found in C9-ALS/FTD cases [31, 52, 69, 73, 97, 119]. The penetrance of the C9-HRE is incomplete and age of onset varies from 40 to 90 years of age [81, 121]. It is therefore difficult to predict if or when C9-HRE carriers will display clinical symptoms. To explore whether cerebral organoids can help to dissect presymptomatic disease mechanisms or act as a platform for (personalized) therapy development, we also generated cerebral organoids from four presymptomatic C9-HRE carriers. Intriguingly, organoids from all C9-carriers showed C9-HRE pathology but the extent to which other cellular and synaptic changes were observed varied for different C9-carriers. Thus, by exploiting a C9-ALS/FTD neural organoid model, that reliably recapitulates C9-HRE molecular pathology, we unveil early changes in cellular architecture and synaptic dysfunction in C9-ALS/FTD that provide a framework for further defining initial disease mechanisms and for designing novel therapeutic strategies for ALS/FTD patients.

Methods

iPSC reprogramming and culture

The different iPSC lines used in this study (generated in the University Medical Center Utrecht or obtained through others) were reprogrammed from skin fibroblasts and blood lymphocytes using Lentiviral, Sendai virus, or episomal plasmid-dependent reprogramming methods [28, 47, 48, 51, 83, 98, 101]. The medical ethical approval committee (METC) of University Medical Center Utrecht granted approval for iPSC line generation through biobank protocol 16–436. Donors gave written informed consent. Patients were diagnosed according to the diagnostic criteria for ALS (revised El Escorial). Details of human subjects and iPSC lines can be found in Supplementary Table 1.

For generating iPSCs at University Medical Center Utrecht, human dermal fibroblasts were obtained from skin biopsies and cultured in Dulbecco's modified Eagles Medium (DMEM; Thermo Fisher Scientific; 41,965,039) supplemented with 10% foetal bovine serum (FBS; Sigma; F7524), 2 mM L-Glu (Gibco; 25,030,024), 100 U/mL penicillin/streptomycin (p/s; Gibco; 15,140,122). Fibroblasts were reprogrammed using the CytoTune-iPS 2.0 Sendai kit (Invitrogen; A16517). Sendai virus was added to the fibroblasts. On day 7 after transduction, cells were plated on MEF-coated culture dishes. After two weeks, ten colonies were picked from each transduction and each clone was expanded separately. From passage 5 onwards, iPSCs were cultured without MEFs. Clones were examined over time and tested for organoid growth potential. The iPSC clones used in this study were extensively characterized using the methods described below.

iPSCs were maintained in StemFlex™ (Life Technologies; A3349401) on Geltrex™ (Gibco; A1413202) coated dishes. iPSCs were passaged once a week using 0.5 mM EDTA. StemFlex was supplemented with 5 μM Y 27632 dihydrochloride (Axon Medchem; 1683) for 24h after passaging to prevent Rho-Kinase-mediated apoptosis. All lines were frequently tested for mycoplasma infection using the MycoAlert kit (Lonza Bioscience, LT07-318).

iPSC characterization

Karyotyping

For karyotyping, 2 million iPSCs (~passage number 10) were plated with 1: Y-27632 dihydrochloride (Tocris, 1254) in StemFlex™ (Life Technologies; A3349401) on GelTrex™ (Gibco; A1413202)-coated dishes. Cells were treated with Colcemid/KCL and fixed. Karyograms of 20 nuclei in metaphase were analysed per iPSC line. GTG (i.e. G-bands by trypsin using Giemsa) was used as a banding method.

Germ layer differentiation

Differentiation of iPSCs into all three germ layers (ectoderm, mesoderm, and endoderm) was performed using STEMdiff™ Trilineage Differentiation Kit (Stem Cell Technologies; 05230), following the manufacturer's guidelines.

Immunocytochemistry

Coverslips were blocked with PBSGT for 30 min at RT and incubated with primary antibodies in blocking buffer overnight at 4 °C. iPSCs: Expression of SOX2, OCT4, TRA1-81, TRA1-60, SSEA4, and NANOG was used to confirm the presence of stem cell markers in iPSCs with StemLight kit (Cell Signalling, 9656S). Differentiated cells: to check pluripotency potential into three germ layers: Brachyury/CD56 for the mesodermal lineage, CXCR4/SOX17 for the endodermal lineage, and PAX6/Nestin for ectodermal lineage (for specific antibodies, see Supplementary Table 5). The next day, coverslips were washed three times with PBS containing 0.5% Triton-X100 and incubated for one hour at RT in secondary antibody dilution (1:750) in blocking buffer. Subsequently, coverslips were incubated with DAPI in PBS (1:1000) for 10 min. Sections were mounted in FluorSave™ Reagent (Millipore, 345789) or Mowiol and stored at 4 °C after drying for one day at RT. Images were obtained with an epifluorescence microscope (Zeiss Axioscope A1) with 20× air objective (NA = 0.5).

Short tandem repeat analysis

iPSCs were harvested as single cells and total double-stranded DNA was extracted using the QuickGene™ DNA kit (Kurabo; DT-S). In short, cells were washed with PBS, lysed in a mix of RNase A (Invitrogen; 12091), Proteinase K and the kit's lysis buffer. After precipitation with 100% ethanol, the lysate was loaded on columns and washed three times. Finally, DNA was eluted and measured on the Qubit™ using the dsDNA BR assay (Invitrogen; Q33266). To amplify the DNA for 9 STR loci (targeting CSF1PO, vWA, TH01, D5S818, D16S539, TPOX, D7S820, D13S317, Amelogenin), the AmpFLSTR™ Identifiler™ PCR amplification kit (Thermo Fisher Scientific; 4365489) was used. Samples were loaded in a 3730 Genetic Analyzer. Per locus, one or two peaks were identified. iPSCs were matched to their parental fibroblast line.

C9 HRE length measurement

Three million iPSCs were harvested as single cells and total double-stranded DNA was extracted using the QuickGene™ DNA kit (Kurabo; DT-S). In short, cells were washed with PBS, lysed in a mix of RNase A

(Invitrogen; 12091), Proteinase K and the kit's lysis buffer. After precipitation with 100% ethanol, the lysate was loaded on columns and washed three times. Finally, DNA was eluted and measured in the Qubit™ using the dsDNA BR assay (Invitrogen; Q33266).

RP-PCR

The presence of C9-HRE was confirmed in C9 iPSCs by repeat-primed PCR (RP-PCR) with the following primers: C9ORF72_RP_PCR_F1: [6FAM]-AGTCGCTAG AGGCGAAAGC, C9ORF72_RP_PCR_R: TACGCATCC CAGTTTGAGACGGGGGCCGG-GGCCGGGGCCGG GG, C9ORF72_RP_PCR_anchor: TACGCATCCCAG TTTGAGACG.

The RP-PCR assay was performed in a mix containing 6.25% genomic DNA (concentration between 61 and 206 ng/µL), FastStart mix (Roche; 4710452001), 875 mM betaine (Sigma; B0300-5VL), 6.25% DMSO (MP Bio; 190186), 1 mM $MgCL_2$ (Bioline; BIO-37026), 187.5 µM 7-deaza-dGTP (Merck; 10988537001), 0.625 µM C9ORF72_RP_PCR_F1 and anchor primer, 0.3125 µM C9ORF72_RP_PCR_R primer in dH20. During PCR, the annealing temperature was gradually decreased from 70 to 56 °C in 2 °C increments with one extra cycle per decrease. After a 15-min incubation at 95 °C, reactions were subjected to 2 to 8 cycles of denaturation at 94 °C for 1 min, 70 °C to 56 °C for 1 min, 72 °C for 3 min, followed by 10 min extension at 72 °C. PCR products were stored at − 20 °C and afterward used for genetic analysis. 1 µL PCR product was combined with 0.1 µL GeneScan™ 500 ROX™ dye Size Standard (Applied Biosystems; 15829716) in 18 µL Hi-Di™ Formamide (Applied Biosystems; 4311320). Fragment length analysis was performed with Peak Scanner v1.0 (Life Technologies) followed by electrophoresis on an automatic sequencer (DNA Analyzer 3730 or 3730XL; Applied Biosystems). A characteristic stutter amplification pattern on the electropherogram was considered diagnostic of a pathogenic repeat expansion.

VNTR-PCR

Repeat length below 30 repeats was determined by variable number tandem repeat PCR (VNTR-PCR). The forward primer was the same as used for RP-PCR, but the reverse primer was different: GCAGGCACCGCAACC GCAG. The assay mix contained 50 ng genomic DNA, FastStart mix, 962 mM betaine, 3.85% DMSO, 385 µM 7-deaza-dGTP, 0.24 µM forward and reverse primer in dH_20. After a 10 min incubation at 95 °C, samples were subjected to 33 PCR cycles with the following settings: 95 °C for 1 min, 60 °C for 1 min, 72 °C for 1 min. This was followed by a 4 min extension at 72 °C. Afterward, samples were kept at 10 °C or stored at − 20 °C and subsequently used for genetic analysis as described for RP-PCR. Repeat length was calculated as the number of bps above 116 bp, divided by the length of the repeat, which is 6. So a peak at 128 bps represents two repeats.

Nanopore sequencing

For measurement of the length of the expanded repeat, high-molecular-weight (HMW) DNA was extracted from three million iPSCs using the Monarch® HMW DNA Extraction Kit for Cells and Blood (New England Biolabs® Inc.; #T3050L) according to the manufacturer's instructions with lysis agitation at 1400 rpm. To decrease viscosity, needle shearing was performed 10 × with a 25G needle and 5 × with a 30G needle. DNA concentration was measured on the Qubit™ using the dsDNA BR assay (Invitrogen; Q33266). DNA integrity was checked with the Agilent 2200 TapeStation System (Agilent; G2964AA) using Genomic DNA ScreenTape (Agilent; 5067–5365) and Genomic DNA Reagents (Agilent; 5067–5366). Depending on the original sample concentration, 2.1–3.3 µg per sample was used for library preparation with the Nanopore Cas9 sequencing kit (Oxford Nanopore Technologies; SQK-CS9109). Three sample preps, each cut with a different pool of four crRNAs (Supplementary Table 5), were pooled before the adapter ligation step and sequenced for 48–72 h on a FLO-MIN106 flow cell (Oxford Nanopore Technologies) with MinKNOW v22.12.5. Fast5 output files were basecalled and mapped to GRCh38 with Guppy v6.1.2, using the Super accurate (SUP) basecalling model. Sequencing reads of multiplexed samples were bioinformatically separated with a custom-made python script. In this step, reads were assigned to a sample based on their mapped start and end positions that correspond to the cut sites of each specific crRNA pool. Repeat length per read was called by STRique v0.4.2 and repeat length of the expanded repeat allele (> 30 repeat units) was visualized in R v4.0. Below 30 repeats was considered a readout of the non-expanded allele.

Cerebral organoid culture

The cerebral organoid protocol used was based on Lancaster & Knoblich (2014) [60]. Small alterations were described previously in Ormel et al. (2018) [83]. Briefly, iPSC colonies were dissociated to single cells using Accutase (Innovative Cell Technologies, Inc.; AT104), cells were counted and seeded in a ULA 96wp (Corning; 7007) at a density of 9k cells per EB in HuES medium (20% KOSR (Gibco; 10828028, 3% FBS (Sigma-Aldrich; F7524), 2mM L-Glu (Gibco; 25030024), 1 × MEM-NEAA (Gibco; 11140035), 3.5 µl/100 mM 2-mercaptoethanol (2ME) in DMEM/F-12) supplemented with 50 µM Y-27632 dihydrochloride (Axon Medchem; 1683) and 4

ng/mL bFGF (Pepro-Tech; 100-18B). The number of live cells was determined using Trypan blue and an automated cell counter. Media was changed every other day, and on day 4 differentiation was started by removing bFGF and ROCK inhibitor. Neural induction started at day 6 with a switch to medium consisting of DMEM/F-12 (Gibco; 11320074) supplemented with 1×N2 supplement (Gibco; 17502001), 2 mM L-Glu (Gibco; 25030024), 1×MEM-NEAA (Gibco; 11140035) and 1 µl/mL heparin (Sigma-Aldrich; H3149). Medium was replaced every other day until pseudostratified epithelium was visible (13 days after seeding). Next, aggregates were transferred to matrigel droplets (Corning; 356234) in 60 mm petri-dishes, as described previously [60]. Media was changed to cerebral differentiation medium consisting of equal parts DMEM/F-12 and Neurobasal (Gibco; 21103,049) medium supplemented with 0.5×N2 supplement, 0,025% human insulin (Sigma; I9278), 2 mM L-Glu (Gibco; 25030024), 0.5×MEM-NEAA, 100 U/mL penicillin/streptomycin (p/s; Gibco; 15140122), 50 mM 2ME and 1×B27 supplement without vitamin A (Gibco, 12587010). After this transfer, aggregates were cultured statically for 4 days to aid the expansion of the neuroepithelium. After two days, medium was replaced with cerebral differentiation medium with 1×B27 supplement (Gibco; 17504044) with vitamin A and dishes were moved to an orbital shaker at 55 rpm. The medium was changed three times a week. At selected time points, organoids were washed with 1×PBS (Thermo Fisher Scientific) and fixed with 4% formaldehyde (Pierce; 11586711) for at least 1 h at 4 °C. After fixation and several PBS washes, organoids were placed in 30% sucrose at 4 °C overnight. Organoids were embedded using O.C.T. compound (Sakura) and stored at − 80 °C until sectioning.

Brightfield image size measurement

Images were taken with an Invitrogen EVOS5000 brightfield microscope. For every organoid batch at least 12 images were taken for every iPSC line at each timepoint (i.e. day 2, 6, and 10). Images were analysed in ImageJ. To determine the EB/organoid area, images were automatically quantified using the Default threshold, which is provided by the software. For statistical analysis, the main effect of disease condition on EB size was determined after a qualitative check for individual cell line and organoid batch effects.

Images of day 90 organoids were taken of organoid dishes placed on graph paper. The organoids were traced manually and the conversion to mm^2 was calculated by dividing with the average value of three squares of 1×1cm of the graph paper.

Size is displayed as a relative measure, where the average of healthy control (HC) is set to 100%.

Immunohistochemistry

Frozen organoid blocks embedded in O.C.T. compound were equilibrated at − 20 °C for 1 h before cryosectioning (Leica Biosystems; CM1950), after which 20 µm serial sections were captured on Superfrost+glasses. Slides were air-dried at RT for at least 1 h and stored at − 80 °C for long-term storage. Sections were washed once with PBS for 10 min before blocking them for 1 h with blocking buffer (10% normal donkey serum (Jackson IR; 017-000-121), 3% BSA (Sigma-Aldrich; A4503), 1% TritonX100 in PBS). Sections were then incubated in primary antibody dilution (for specific antibodies, see Supplementary Table 5) in blocking buffer overnight at 4 °C. The next day, sections were washed three times with PBS and incubated for 1 h at RT in secondary antibody dilution (1:750) in blocking buffer. Subsequently, they were incubated with DAPI in PBS (1:1000) for 15 min. Sections were mounted in FluorSave™ Reagent (Millipore, 345789) or Mowiol and stored at 4 °C after drying for one day at RT. Images were obtained with a confocal microscope (Olympus LS FV1000) using the UPlanSApo 100×oil objective (NA = 1.40) and Z-stack step size of 0.34 µm for the RNA foci staining. MAP2/KI67 images were obtained with an epifluorescence microscope (Zeiss Axioscope A1) with 20×air objective (NA = 0.5).

Quantitative real-time PCR

Organoids were lysed in QIAzol reagent (Qiagen; 79306) and mechanically dissociated using an Ultra-Turrax (IKA; T10). Chloroform (1:6, Riedel-de Haën, 32211) was added to the tubes, before being rotated a few times and incubated at RT for 3 min. Samples were then centrifuged at 12,000 g, and the aqueous phase was used for RNA extraction. Total RNA was isolated using the RNeasy mini kit (Qiagen; 74104). RNA quality and purity were analyzed in the NanoDrop™ 2000. Total RNA (500 ng) was used for cDNA synthesis using the Superscript IV kit (Invitrogen; 18090200) according to manufacturer's instructions. RT-qPCR with the SYBR™ green (Roche) dye as a detection system was carried out in the Quantstudio™ 6 Flex Real-Time PCR system (Applied Biosystems) with the following temperature settings: 50 °C for 2 min, 95 °C for 10 min, then 40 cycles of 15 s at 95 °C and 60 s at 60 °C. Sense and antisense primers (designed or checked for specificity with the online primer BLAST design tool, NCBI) were combined to make the primer mixes (for primer sequences see Supplementary Table 5). Samples were tested in duplicates. *RPII* and *TBP* were used as reference genes to standardize the measured expression level. Relative expression was calculated using the ΔΔCT method. Melt curves of the PCR product were inspected for the presence of primer

dimers. For statistical analysis, we corrected for multiple testing. Each sample contained at least 3 organoids.

Western blot analysis

Relative C9ORF72 protein levels in C9 organoids and healthy controls were determined. Samples consisting of three organoids (day 45) were lysed-homogenized in RIPA buffer (300 µl TBS with 1% NP40, 1% sodium deoxycholate, 0.1% SDS) with cOmplete™ protease inhibitor (Roche, 11836170001) using Ultra-Turrax® (IKA, T10). Lysates were run through a syringe (25G) to break down DNA. They were then placed in a rotor for 20 min and centrifuged at 13.200 RPM for 20 min at 4 °C. The supernatant (soluble phase protein) was collected and stored at − 80 °C. Before gel loading, protein samples were diluted in loading buffer (2% SDS, cOmplete™ protease inhibitor) and an equal volume of each sample was added to a lane on each of two 10% polyacrylamide gels. The gel was run at 90V for 30 min to facilitate proper stacking of the protein, after which the voltage was increased to 120V until the protein arrived at the bottom of the gel. The proteins were then transferred to a Protran® 0.45um nitrocellulose membrane (Cytiva™, 10600002) by wet blotting at 100V for 60 min. Next, the blot was incubated in blocking mix (0.25% gelatine in 0.5% TBS-Triton X-100, pH 7.4) for 10 min and incubated with a mouse α-C9ORF72 primary antibody (1:1000, GeneTex, GTX632041) and a chicken α-GAPDH primary antibody (1:1000, Abcam, ab14247) or a rabbit α-GAPDH primary antibody (1:1000, Abcam, ab9485) overnight at 4 °C on a shaker. The next day, blots were washed with 0.05% TBS-Tween 20 (TBS-T), and incubated with α-mouse IRDye 800 secondary antibody (1:2500) and α-chicken or α-rabbit Alexa Fluor™ 647 secondary antibody (1:1000). Then, after washing with TBS-T, blots were scanned with the Odyssey® CLx imaging system (LI-COR Biosciences) at 700 nm and 800 nm. Quantification of C9ORF72 and GAPDH protein expression was done using Image Studio Lite v5.2 (LI-COR Biosciences) and FIJI (ImageJ). C9ORF72 expression was normalized to GAPDH expression in the same lane. These values were additionally normalized to the average C9ORF72 expression of three healthy control organoid samples Statistical analysis was performed in GraphPad Prism 8.4.2. with an One-tailed t-test.

LNA-FISH

Locked nucleic acid (LNA) fluorescence in situ hybridization (FISH) was performed as described [53]. Briefly, fresh-frozen or PFA-fixed organoids were cut into 20 µm thin sections on a Leica Cryostat. Glass slides were stored at − 80 °C until use. After pre-fixation (4% PFA for 10 min at RT), sections were acetylated (10 min at RT) and permeabilized with proteinase K (5 µg/ml for 5 min at RT). Prehybridization with hybridisation buffer for 1 h at RT was followed by the hybridization with 40 nM of a custom-made 3′ and 5′ DIG-labelled probe against the sense C9ORF72-HRE (Sequence: CCCGGCCCCGGC CCC, Qiagen) or a Scrambled control (Qiagen), overnight (ON) at 45 °C. Before hybridization, probes were denatured for 30 min at 65 °C in hybridization buffer and quickly placed on ice. The next day, tissue slides were washed once with 5×SSC for 5 min and incubated in 0.2×SSC for 1.5 h at 50 °C, followed up with eight washes for 10 min each in B1 solution (0.1 M Tris, pH 7.5, 0.15 M NaCl) supplemented with Tween (0.0005%). For immunohistochemistry and ISH, slides were blocked in 10% FBS in B1 buffer with Tween (0,0005%) for 1 h at RT and subsequently incubated with anti-DIG-POD (1:500; Roche Diagnostics; 11207733910) and chicken anti-MAP2 (1:1000; Abcam; ab92434) antibodies in 1% BSA, 0.3% Triton-X-100 in 1×PBS ON at 4°C. The next day, tissue slides were washed three times with B1 solution for 5 min each, followed by incubating with TSA™ Cyanine 3 reagent (1:50 in amplification diluent; AKOYA Biosciences; SAT704A001EA) for 10 min at RT. Then washed four times for 5 min each in B1 buffer supplemented with 20% Tween followed by incubation with secondary antibody donkey-anti-chicken-Alexa Fluor™ 488 (1:750; Invitrogen) in 1×PBS for 1 h at RT. Finally, tissue slides were washed twice for 5 min each with 1×PBS, incubated with 1×DAPI for 10 min at RT to stain the nuclei, and washed once for 5 min with 1×PBS. Slides were mounted with FluorSave™ reagent (Millipore) and images were acquired on a confocal microscope (Zeiss) with image acquisition software (Zen 3.3, Zeiss).

MSD immunoassay

A poly(GP) and poly(GA) Meso Scale Discovery (MSD) immunoassay was performed on brain organoids after lysis in RIPA buffer containing 2% SDS (Fisher Bioreagents, BP166-100) and 2×cOmplete Protease Inhibitor Cocktail (Roche, 11836170001) and mechanical dissociation using an UltraTurrax (IKA; T10). Samples were then sonicated (3×5 s) at 4 °C and centrifuged at 17,000×g for 20 min at 16 °C. Supernatant was collected and frozen at − 80 °C. An aliquot was taken from each sample before freezing to perform a Pierce™ BCA Protein Assay (Thermo Fisher Scientific, 23227).

MSD immunoassay was performed in single-plex using 96-well SECTOR plates to quantify endogenous poly(GP) and poly(GA) expression levels in the brain organoids, as previously described [103]. For poly(GP) immunoassays, samples were loaded at 45 µg protein per well, while for poly(GA), 27 µg protein was loaded. Prior to analysis, the average reading from a calibrator containing no peptide

was subtracted from each reading. See Supplementary Table 5 for reagents and antibodies used.

scRNA sequencing

Organoid dissociation to single-cell suspension

After washing with PBS, eight organoids were cut into small pieces. Then, papain (Worthington; LK003178) and DNAse I (Worthington; LK003172) were mixed in DMEM/F-12, added to the organoids, and then this mix was put on an orbital shaker at 50 rpm to incubate for 25 min in total at 37 °C. Every 10 min, the cell suspension was vigorously pipetted up and down. Afterwards, the reaction was quenched with DMEM/F-12 supplemented with 2% FBS. Doublets and clumps were removed with cell strainers: first with those containing 100 µm pores and then 70 µm pores. Finally, the cell suspension was centrifuged for 5 min at 300 rcf and resuspended in 250 µl mix of DMEM/F-12 with 40% FBS, counted and checked for cell viability, and then frozen in DMEM/F-12 with 40% FBS and 15% DMSO.

Library preparation and sequencing platform

Cells were sequenced by Single Cell Discoveries (Utrecht, The Netherlands) according to the 10X Genomics single cell 3' gel bead kit version 3 (Chromium Next GEM Single Cell 3' GEM, Library & Gel Bead Kit v3). In short, cell suspensions were thawed, and the cells were washed and filtered one more time to ensure single cells. Cells were put on a Chromium single cell 3' chip, where single cells were linked to a Single cell 3' v3 gel bead and were separated from other cells by oil. Then, beads were dissolved, primers were released and the cell was lysed. The beads were coated with strands containing an Illumina TruSeq read 1, a 16 nucleotide (nt) 10X barcode, a 12 nt unique molecular identifier (UMI), and a 30 nt poly(dT)VN tail. The poly-A tails of the mRNA molecules aligned with the poly-T tails. The barcode diversity was 3.5 million. There was a different barcode per cell and a different UMI per mRNA molecule. The DNA primer was elongated to match the mRNA molecule by reverse transcription followed by template switch oligo priming and mRNA transcript extension. Then, single-cell partitions were pooled again. Silane magnetic beads were used to extract the first-strand cDNA and the barcoded cDNA was amplified by PCR to complete the library preparation. P5, P7, a sample index, and TruSeq Read 2 (read 2 primer sequence) were added via End Repair, A-tailing, Adaptor Ligation, and PCR. The final libraries contained the P5 and P7 primers used in Illumina bridge amplification. The 16 bp 10×Barcode and 12 bp UMI were encoded in Read 1, while Read 2 was used to sequence the cDNA fragment. Sequencing was performed on Illumina NextSeq 2000. Sequencing depth was set at 50,000 reads per cell for 5,000 cells per sample.

Mapping, read alignment, data filtering, and normalization

Only reads containing a barcode and UMI were considered. The barcodes gave a number of unique molecular identifiers (UMIs) per cell, which constitutes the read count per cell. The counts contain both spliced, mRNA molecules with a poly-A tail, as well as unspliced, pre-RNA molecules with a poly-A stretch in their introns, RNA reads. The reads were aligned to the human genome (Ensemble GRCh38) using the cellranger (v4.0.0) pipeline. The count files were used as input for the Scanpy (v1.8.1) pipeline [117, 118, 122].

Data filtering

Before processing, 31.420 cells and 36.601 genes were identified. After removal of mitochondrial genes, cells had a median of around 1460 genes and 2315 UMIs per cell. A threshold was set to include cells that contained more than 100k reads, 20% mitochondrial counts, and 50% ribosomal counts. We also filtered for minimal1000 genes per cell and only genes that were expressed by at least 0.1% of cells. After filtering, 25.126 cells remained.

Normalization

Normalization was performed using sc.pp.normalize_total() whereby each cell had the same total count. Then the data matrix was logarithmized using sc.pp.log1p(). Highly variable genes were annotated using sc.pp.highly_variable_genes() using default settings. Non-variable genes were removed and 21.113 cells and 31.989 genes were retained in the dataset.

Principle component analysis

Principle components were computed using sc.tl.pca() with svd_solver = 'arpack'. The k nearest neighbors was calculated with default settings and used to plot UMAPs [75].

Cell type annotation

Leiden (v0.8.4) clusters were calculated with default parameters [108], which yielded 28 clusters. Data were loaded from E-MTAB-7552 [56]. The top 100 genes that characterized each cluster by the Wilcoxon-rank-sum test were extracted using the sc.tl.rank_genes_groups() function in Scanpy on the cl_FullLineage parameter from their metadata. ScoreCT (https://github.com/LucasESBS/scoreCT) was used to transfer labels from the Kanton cell types to our Leiden clusters. The Wilcoxon method was used to rank genes of the Leiden clusters. Labels were checked and label names were refined based on the top 100 genes defining that cluster. Similar

clusters were grouped for higher analysis power, e.g. radial glia 1 and 2 were merged. Supplementary Table 2 recorded this annotation process from Leiden clusters to final annotation.

Composition analysis

scCODA (v0.1.4) was used to visualize and analyse the composition of our samples [22]. Line and condition were given as covariates.

Differential gene expression

Gene expression was compared between C9 and HC organoids within cell-type clusters with the Wilcoxon-rank-sum test using the sc.tl.rank_genes_groups() function in Scanpy. A cutoff of p_adjusted < 0.01 was used, but no cut-off for the log fold change. This yielded a list of differentially expressed genes (DEGs) that were up- or downregulated per cluster. The genes can be retrieved in Supplementary Table 3.

Gene set enrichment analysis

DEGs were analysed for gene set enrichment using EnrichR in the gseapy (v0.10.5). DEGs were compared to the human KEGG 2021 database [54, 55]. Unique genes in the current dataset were used as the background for the analysis. The complete dataset of KEGG terms up- or downregulated in C9 per cell type can be found in Supplementary Table 4.

Gene expression omnibus

The scRNA-seq data discussed in this publication have been deposited in NCBI's Gene Expression Omnibus [32] and are accessible through GEO Series accession number GS264012 (https://www.ncbi.nlm.nih.gov/geo/query/acc.cgi?acc=GSE264012).

Other software packages and versions

Python = = 3.8.8, anndata = = 0.7.6, matplotlib = = 3.4.3, numpy = = 1.21.2, pandas = = 1.3.3, psutil = = 5.8.0, scipy = = 1.7.1, tables = = 3.6.1.

3D fluorescent light sheet microscopy

At least three brain organoids per iPSC line were fixed in 4% PFA for 1-3h at 4 °C and washed multiple times in PBS. The iDISCO clearing procedure was performed as described [90, 91]. Brain organoids were immersed for 24h in permeabilization solution (2.3% m/vol glycine, 20% DMSO, 0.2% TritonX-100 in PBS) at 37 °C. Then the solution was exchanged for blocking solution (6% normal donkey serum, 10% DMSO, 0.2% TritonX-100 in PBS) for 24 h at 37 °C. Next, organoids were incubated for 4 days at 37 °C with primary antibodies (Supplementary Table 5) in PBS with 3% normal donkey serum, 5% DMSO, 0.2% Tween-20, and 10 µg/mL Heparin. Then, samples were extensively washed in PBS with 0.2% Tween-20 and 10 µg/mL Heparin. They were incubated for 3 days at 37 °C with the secondary antibodies (Supplementary Table 5) in PBS with 3% Donkey serum, 0.2% Tween-20, and 10 µg/mL Heparin. The solution with secondary antibodies was filtered with a 0.22 µm filter before use. To-Pro3 (Topro3) nuclear fluorescent dye (1:5000; Thermo Fisher Scientific, T3605) was used to stain nuclei. The next day, samples were washed extensively with PBS containing 0.2% Tween-20 and 10 µg/mL Heparin.

For tissue clearing, samples were embedded in 1% agarose in TAE and subsequently dehydrated in a methanol/H2O series at RT. Then samples were incubated ON in a mix of 66% dichloromethane (DCM; Sigma, 270997) and 33% Methanol at RT. Afterward, samples were incubated twice in 100% DCM for 15 min. Finally, samples were put in dibenzylether (DBE; Sigma, 108014) for at least one day.

Brain organoids were imaged with an Ultramicroscope II (LaVision BioTec) fluorescent light sheet microscope equipped with an MVX-10 Zoom Body (Olympus), MVPLAPO 2×Objective lens (Olympus), Neo sCMOS camera (Andor) (2560×2160 pixels. Pixel size: 6.5×6.5 µm^2) and Imspector software (version 5.0285.0) (LaVision BioTec). Samples were scanned with single-sided illumination, a sheet NA of 0.148348 (results in a 4 µm thick sheet) and a step-size of 2.5 µm using the horizontal focusing light sheet scanning method with 6 steps combined with the blend algorithm. A dipping cap correction lens (LV OM DCC20) was included in the object lens (working distance = 5.7 mm). This resulted in an effective magnification of 3.44×(= Zoom Body•Objective + Dipping lens = 1.6×•2.152×). For imaging the following laser filter combinations were applied: Coherent OBIS 488–50 LX Laser with 525/50 nm filter, Coherent OBIS 561-100 LS laser with 615/40 nm filter, Coherent OBIS 647-120 LX laser with a 676/29 nm emission filter and Coherent OBIS 730-30 LX Laser with a 775/50 nm emission filter.

Stem cell pool quantification in Imaris

SOX2-positive ventricle-like structures were analysed in Imaris 9.8.2. using the surface analysis feature. Throughout the 3D-tissue of the sample, approximately 1000 slices could be made. Every 5 steps, the ventricle-like structures were manually traced by following the Topro3-positive areas, as the signal was more distinguishable than SOX2. However, it was always checked whether SOX2 was present. The presence of ZO-1 signal was also used, as this is a marker for the lumen edge of the ventricle. The inside of the ventricle (lumen) was not taken into consideration, so both the outside of the structures was

traced as well as the ZO-1 signal to create a 3D-blob of only the SOX2-positive cells. The total volume of these 3D-volumes was summated for each organoid to create a total volume of SOX2-positive ventricle-like structures. The total volume of the organoids was also measured in Imaris 9.8.2. with an automatic surface analysis in the autofluorescence channel. After this, a ratio could be made of the ventricle-like structures compared to the total size of the organoid. The total volume of the organoids was compared between lines, as well as the SOX2% of the entire volume and the SOX2% of the three largest ventricles per organoid.

Synapse quantification

Confocal data were analyzed for synaptic puncta with the ImageJ ComDet v.0.5.5. plugin specialized in the detection of particles [57]. Values for parameters, such as particle size, intensity threshold, and the colocalization distances, were based on literature [40]. Values for the number of puncta and the size of the puncta were provided by the plugin. For the non-synaptic measurements, the analysis pipeline is displayed in Supplementary Fig. 7b. In short, the number of puncta was normalized against the area of MAP2 in the image, which is indicative of the density of the dendritic network. MAP2 signal and the puncta were manually thresholded in ImageJ. The intensity of the signal was measured inside these two selection areas in their respective channels. Next, puncta were omitted from the image. Afterward, the SYP and SHANK2 intensity was measured inside the MAP2-selection. The background signal, i.e. the signal area outside the MAP2 selection, was subtracted. This resulted in a non-synaptic measurement of SYP and SHANK2. Results were compared with an Unpaired T-test in GraphPad Prism 8.4.2 to test for significant differences between groups, or a Mann–Whitney Test if required assumptions for normality and/or homogeneity of variance were not met. Said assumptions were checked with a QQ-plot, a homoscedasticity plot, and a residual plot.

Whole-cell patch-clamp recordings in ALI-COs

Whole-cell patch-clamp recordings were conducted on air–liquid interface (ALI) cerebral organoids (COs). ALI-COs were obtained from day 55 cerebral organoids, as previously described [44] using a VT1000S vibratome (Leica). At 105 ± 15 days, ALI-COs were transferred to a recording chamber filled with artificial cerebrospinal fluid (aCSF) containing (in mM, 300 mOsm, pH adjusted 7.35) 124 NaCl, 2.5 KCl, 1 NaH_2PO_4, 26 $NaHCO_3$, 2.5 $CaCl_2$, 1.3 $MgCl_2$, 5 HEPES, and 11 Glucose at 37 ± 1 °C. An upright microscope (SliceScope Pro 6000, Scientifica) with oblique illumination and a 40× water immersion objective was used to visualize cells. Cells were patched using borosilicate glass (Science Products) electrodes (3—5 MΩ) containing (in mM, 300 mOsm, pH adjusted 7.3) 139 K-Gluconate, 5 KCl, 10 HEPES, 10 Phosphocreatine, 2 $MgCl_2$, 4 Na-ATP, 0.3 Na-GTP and 0.2 EGTA. 0.5% biocytin was additionally added to the pipette solution to facilitate visualization of recorded cells afterward. Cells were patched near the ALI-CO border at -60 mV resting membrane potential in voltage-clamp (vc) configuration. After break-in, the resting membrane potential was assessed in current-clamp (cc) configuration. Cells with a resting membrane potential > − 20 mV were excluded from analysis. Cells were then allowed to rest for 2 min in vc configuration to ensure stability of the recording. Spontaneous excitatory postsynaptic currents (sEPSCs) were recorded at a membrane potential of − 60 mV for 10 min. The excitability was determined in cc configuration. Current injections were used to evoke action potential firing (500 ms pulses, − 20 to + 60 pA, + 5 pA increments). Recordings were performed in this same order for all cells. Series resistance was monitored throughout the recording and cells with a series resistance of > 25 MΩ were excluded from analysis. All obtained recordings were amplified and low-pass filtered at 5 kHz using an Axopatch 200B amplifier (Molecular Devices). Recordings were digitized (Axon Digidata 1550B, Molecular Devices) and stored using pClamp 10.6 software (Molecular Devices). Data were analyzed using Clampfit 10.6 (Molecular Devices). The recording aCSF was continuously perfused with 95% O2 and 5% CO2.

Cell cycle phase analysis

The cell cycle profile was analysed as previously described [99]. Following manufacturer's instructions of the Click-iT™ EdU Alexa Fluor™ 647 Flow Cytometry Assay Kit (Invitrogen, C10424), iPSCs were incubated with 10μ M EdU for 45 min at 37 °C and 5% CO2. Cells were then washed with PBS, incubated with Accutase for 2 min, and suspended in HuES medium. Samples were then washed in 1% BSA in PBS. Cells were fixed for 10–15 min by adding Click-iT fixative at RT followed by washing with 1% BSA in PBS and permeabilization with saponin for 15–30 min at RT. Cells were incubated with Click-iT reaction cocktail (2% CuSO4, 0.5% Fluorescent dye azide, 10% Reaction buffer additive, in PBS) for 30 min at RT in the dark followed by a wash with Click-iT saponin-based permeabilization and wash reagent. Samples were then stained with DAPI 30 min at RT. Afterward, the cell cycle was analysed using fluorescence activated cell sorting (FACS; BD FACSCanto II) for 10,000 events per cell line. Cell cycles were assigned after filtering for live cells based on the FSC/SSC in the BD FACSDiva software.

Results

C9-ALS/FTD cerebral organoids show all three C9-HRE pathological hallmarks.

Repeat-primed PCR and nanopore sequencing confirmed that, as expected, healthy control (HC) and C9-isogenic cells had < 30 HRE repeats on both alleles, while C9-ALS/FTD (C9) iPSCs had an expanded repeat on one allele with a median length between 809 and 1175 repeats (Fig. 1a, Supplementary Table 1). Next, organoids were generated as reported previously (Fig. 1b, Supplementary Fig. 1a) [60, 83]. At day 45, HC and C9 organoids displayed ventricular-like zones (VLZs) with KI67$^+$ proliferative cells surrounded by MAP2$^+$ neural regions (Fig. 1c, Supplementary Fig. 1b). Interestingly, while in HC organoids KI67$^+$ cells were mostly confined to the inner part of the VLZ, these cells were more broadly distributed in C9 organoids. Quantitative PCR (qPCR) showed comparable expression for the neuronal cytoskeleton marker *TUBB3* and early born neuron marker *DCX* (Fig. 1d; Unpaired two-tailed t-test, *TUBB3*: $t(29) = 0.03452$, $p = 0.9727$; DCX: $t(29) = 1.818$, $p = 0.0795$). Thus, while at day 45 the overall cytoarchitecture of HC and C9 organoids was similar and in line with previous studies (e.g. [60, 83]), the distribution of KI67$^+$ cells was more widespread in C9 conditions.

To further characterize the C9 organoid model, we examined the different types of molecular pathology associated with C9-HRE [72]. First, Western blot analysis showed a ~ 30% reduction in C9ORF72 expression in C9 versus HC organoids at day 45 (Fig. 1e; One-tailed t-test, $t(18) = 4.141$, $p = 0.0003$). Second, MSD-ELISA assays confirmed the presence of glycine-proline (GP) and glycine-alanine (GA) DPRs in day 90 C9 but not HC organoids (Fig. 1f). Poly(GP) and poly(GA) are most abundant in C9 brain tissue and the only DPRs that can be quantified using this assay [7, 71, 80]. Third, LNA-FISH using a probe targeting the sense repeat (GGGGCC) identified sense RNA foci in some but not all cells in day 90 C9 organoids, in line with previous observations in other tissues [7]. No RNA foci were observed in HC organoids and no signal was found in C9 organoids incubated with a scrambled probe (Fig. 1g, Supplementary Fig. 1c). Thus, while previous work reported poly(GA) in matured (day 150) organoid slices [107] our experiments show all three reported molecular pathologies associated with C9-HRE, including multiple DPRs, at earlier stages of C9 cerebral organoid development.

C9-HRE causes early accelerated cerebral organoid growth

Having established the presence of molecular pathology in C9-ALS/FTD cerebral organoids, we next explored the effect of C9-HRE at different stages of organoid development. First, early stages were assessed, as C9-HRE was reported to affect early developmental processes, such as stem cell proliferation, in cultured cells and mice [48]. Analysis of organoid (embryoid body) size at day 2, 6, or 10 after iPSC seeding revealed a significant increase in the cross-sectional area of C9 versus HC organoids at day 6 and 10 (Fig. 2a, b, two-way ANOVA with Šídák's correction for multiple testing, $F(1,1725) = 77.91$, $p < 0.0001$; Supplementary Fig. 2a). To determine whether this change is C9-specific or represents a more general ALS/FTD phenotype, cerebral organoids were generated from 1) matching C9 isogenic control (C9-iso) lines, or 2) from iPSCs carrying other ALS mutations (TDP43-ALS, carrying M337V or I383T mutations, and ATXN2-ALS, carrying an intermediate CAG repeat expansion; Supplementary Table 1).

PCR confirmed lack of C9-HRE in C9-iso lines (Supplementary Table 1), and immunohistochemistry and qPCR showed an overall cytoarchitecture and marker expression in C9-iso organoids that resembled HC (Supplementary Fig. 2b–e). Comparison of the size of HC, C9, and C9-iso organoids showed significant differences between the groups at day 10 (Fig. 2c, d, one-way ANOVA with Dunn's correction for multiple testing, $F(2,732) = 51.54$, $p < 0.001$). C9 organoids were larger than HC ($p_{adj} < 0.001$) and C9-iso ($p_{adj} = 0.012$), while C9-iso organoids were only slightly, but significantly, larger than HC ($p_{adj} = 0.019$). Size measurements of organoids with different genetic backgrounds showed significant differences at day 10 (one-way ANOVA with Tukey's correction for multiple testing, $F(3,633) = 42.41$, $p < 0.001$). C9 organoids were significantly larger than ATXN2-ALS ($p_{adj} < 0.001$), TDP43-ALS ($p_{adj} < 0.001$), and HC ($p_{adj} < 0.001$) organoids. The size of ATXN2-ALS, TDP43-ALS and HC organoids was similar (ATXN2-TDP43: $p_{adj} = 0.443$; ATXN2-HC: $p_{adj} = 0.858$; TDP43-HC: $p_{adj} = 0.065$; Fig. 2e, f). Thus, the early accelerated growth of C9 organoids is at least partially caused by HRE and is not observed in several other genetic ALS backgrounds (TDP-43-ALS, ATXN2-ALS). Finally, organoid size was determined at a later stage of organoid development, at day 90, which relates to a developmental stage at which various neuronal subtypes and astrocytes are present [14, 25, 110]. In contrast to early stages, C9 organoids were significantly smaller as compared to HC at day 90 (Fig. 2g, h, Mann–Whitney t-test, $U = 2.402$, $p < 0.0001$), a phenotype that was not observed in C9-iso organoids (data not shown).

Together, these data reveal opposite size phenotypes in C9 organoids at different developmental stages.

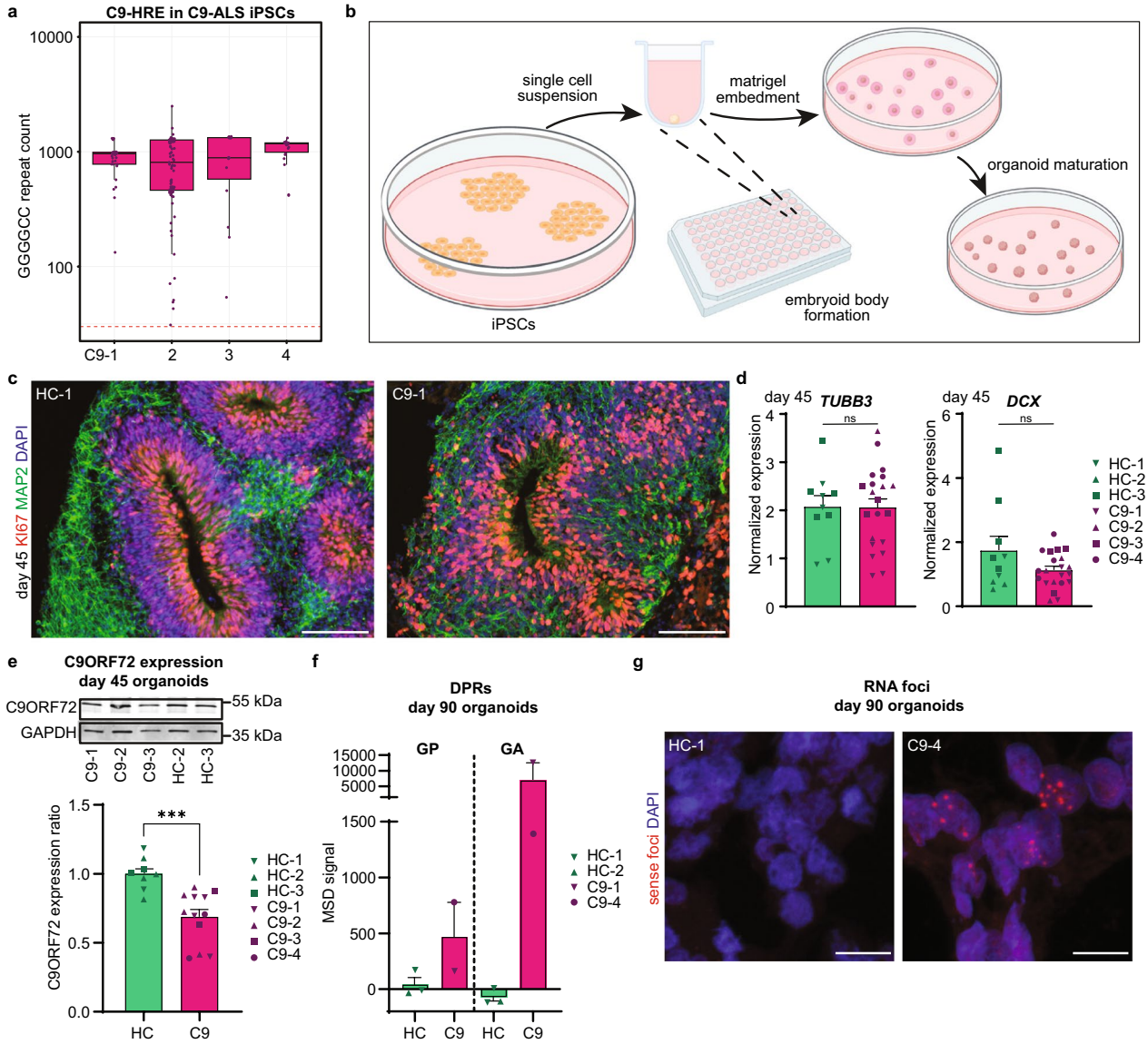

Fig. 1 C9-ALS/FTD cerebral organoids show all three *C9ORF72-HRE* pathological hallmarks. **a** Nanopore sequencing of iPSCs from different C9-ALS/FTD patients (C9-ALS-1-4, Supplementary Table 1) to determine GGGGCC repeat count. Dots represent individual reads, on which the box and whiskers plot is based. Red-dotted line indicates the 30-read cut-off used to separate the reads of the expanded and non-expanded allele. **b** Schematic illustration of the cerebral organoid culture method [60, 83]. **c** Representative image of immunohistochemistry on cryosections of day 45 cerebral organoids from a healthy control (HC) and C9 patient for MAP2 (green; neuronal part) and KI67 (red; ventricular-like zone) in combination with DAPI to mark nuclei. **d** Quantitative PCR for the neuronal cytoskeleton marker *TUBB3* and early-born neuron marker *DCX* in day 45 C9 and HC organoids. Expression is normalized to *TBP* and *RPII*. Data are shown as the mean ± SEM, symbols indicate specific lines and dots represent ≥ 3 pooled organoids. 2–6 independent organoid differentiations were performed per iPSC line, every data point is the average of two technical replicates. Unpaired two-tailed t-test, *TUBB3*: $t(29) = 0.03452$, $p = 0.9727$; DCX: $t(29) = 1.818$, $p = 0.0795$. **e** Example of Western blot analysis of C9ORF72 expression in day 45 C9 and HC organoids. Data in graph indicate the mean ± SEM (normalized to GAPDH), symbols indicate specific lines and dots represent individual Western blot measurements of ≥ 3 pooled organoids. 1–2 independent organoid differentiations were performed per iPSC line with 2 technical replicates per sample. Unpaired one-tailed t-test, $t(18) = 4.141$, $p = 0.0003$. **f** Poly(GP) and poly(GA) levels were measured in day 90 organoids from HC and C9 patients. Data are shown as the mean ± SEM, symbols indicate specific lines and data points represent individual MSD measurements of ≥ 3 organoids pooled per experiment after background subtraction. **g** Representative images showing LNA-FISH for sense RNA foci (red) in cryosections of day 90 HC and C9 organoids. DAPI (blue) marks nuclei (n = 1 HC, n = 2 C9 lines). Scrambled control probes did not show signal (Supplementary Fig. 1c). Scale bars: **c** 100 µm, **g** 10 µm. *** = $p < 0.001$

C9-HRE causes a reduction of deep layer neurons and disorganized radial glia

The reduced size of C9 organoids at day 90 may reflect changes in specific cell populations. Therefore, to study the cell types present at day 90 single-cell RNA sequencing (scRNA-seq) was performed on HC (n = 3 lines) and C9 (n = 3 lines) organoids (Fig. 3a). After quality control, 21.113 cells expressing 31.989 genes were retained (Supplementary Fig. 3a–f). Principle component analysis (PCA) was performed followed by a computation of nearest neighbours and visualization using UMAP. Cells from HC and C9 organoids were mixed between batches and lines (Supplementary Fig. 3g–h). To identify cell types, PCA data was used as input for the Leiden algorithm [108] function in Scanpy [117, 118, 122], which yielded 28 clusters (Fig. 3b). No obvious differences in the distribution of HC and C9 cells over clusters were identified (Fig. 3c). To aid unbiased annotation of 28 clusters identified through our computational pipeline (Fig. 3b, see Methods), data were compared to a large scRNA-seq cerebral organoid dataset covering stages up to day 120 [56]. Cell types in day 90 HC and C9 organoids ranged from radial glia and neurons to choroid plexus, endothelial cells, and oligodendrocyte precursors (Fig. 3d–f, Supplementary Fig. 3i). Clusters that belonged to the same cell type were grouped, e.g. radial glia 1 and 2 were merged (Supplementary Table 2). One C9 sample contained retinal pigment epithelial cells. These cells infrequently form [60] and were excluded from the grouped compositional analysis (Fig. 3d, g). Differences in cell type abundance in HC and C9 organoids were found at day 90, although these changes were not statistically significant. Nevertheless, overall changes in the contribution of specific cell types were observed, including a relatively larger contribution of (upper layer) neurons, glia/astrocytes, a smaller contribution of deep layer neurons, and changes in radial glia clusters in C9 as compared to HC organoids (Fig. 3g, Supplementary Fig. 3j).

The identification of the same cell types in both HC and C9 samples allowed us to compare differences in gene expression within each cell type. Significantly up- and down-regulated genes in C9 as compared to HC samples were subjected to pathway analysis (Supplementary Table 3). This revealed enrichment of specific KEGG pathways in distinct cell types (Fig. 3h). Several of these pathways had previously been linked to ALS, e.g. nicotine addiction, axon guidance, glutamate synapse, ALS, oxidative phosphorylation, and regulation of actin cytoskeleton (Supplementary Table 4). Overall, these results suggest changes in the abundance or distribution of specific cell types in day 90 C9 organoids together with cell type-specific changes in gene expression.

To confirm and follow up on the scRNA-seq data, deep layer neurons were assessed using immunohistochemistry. C9 organoids showed a reduced contribution of deep layer neurons (Fig. 3g, Supplementary Fig. 3k), which are a known vulnerable population in ALS/FTD and include upper MNs [4, 70, 78, 79, 96, 102]. CTIP2 marks excitatory deep layer neurons and is important for the specialization of subcerebral projection neurons, which give rise to upper MNs (also called corticospinal MNs) and corticotectal projection neurons [70]. Day 90 HC organoids displayed highly organized VLZs, surrounded by a dense $MAP2^+$ neuronal network and many $CTIP2^+$ deep layer neurons. In contrast, in C9, but not C9-iso, organoids the number of $CTIP2^+$ neurons were drastically lower (Fig. 4a,). Moreover, qPCR analysis of day 90 HC and C9 organoids from multiple inductions independent of the scRNA-seq experiment confirmed a decrease in *CTIP2* mRNA (Fig. 4b, Mann–Whitney t-test, $U = 7$, $p = 0.0005$). This reduction likely arises at early developmental stages as *CTIP2* mRNA was already decreased at day 45 in C9,

(See figure on next page.)

Fig. 2 C9-HRE causes stage-dependent changes in organoid size. **a** Representative brightfield images of healthy control (HC) and C9-ALS/FTD (C9) cerebral organoids at day 2, 6, and 10. **b** Quantification of the cross-sectional area of HC and C9 organoids at day 2, 6, and 10 based on images as in a. Size normalized to the HC average. Graph shows mean ± SEM, n = 12 organoids per timepoint from 3 to 6 independent differentiations per iPSC line (n = 3 HC, n = 4 C9 lines), two-way ANOVA with Šídák's correction for multiple testing, $F(1,1725) = 77.91$, $p_{adj} < 0.0001$. **c** Representative brightfield images of HC, C9, and corresponding C9-isogenic control (C9-iso) organoids at day 10. **d** Quantification of the cross-sectional area of HC, C9, and C9-iso organoids at day 10 based on images as in (**c**). Size normalized to the HC average. Graph shows mean ± SEM, n = 12 organoids from 3 to 6 independent differentiations per iPSC line (n = 3 HC, n = 4 C9, n = 3 C9-iso lines), one-way ANOVA with Dunn's correction for multiple testing, $F(2,732) = 51.54$, $p_{adj} < 0.001$. **e** Representative brightfield images of C9, ATXN2-ALS (ATXN2) and TDP43-ALS (TDP43) organoids at day 10. **f** Quantification of the cross-sectional area of HC, C9, ATXN2, and TDP43 organoids at day 10 based on images as in e. Size normalized to the HC average. Graph shows mean ± SEM, n = 12 organoids from 3–6 independent differentiations per iPSC line (n = 3 HC, n = 4 C9, n = 5 ATXN2-ALS, n = 2 TDP43-ALS lines), one-way ANOVA with Tukey's correction for multiple testing, $F(3,633) = 42.41$, $p_{adj} < 0.001$. Non-significant comparisons are not displayed in the graph. **g** Representative brightfield images of HC and C9 organoids at day 90. **h** Quantification of the cross-sectional area of HC and C9 at day 90 based on images as in g. Size normalized to the HC average. Graphs show, mean ± SEM, measurements from 3–6 independent differentiations per iPSC line. n = 3 HC, n = 4 C9 lines, Mann–Whitney t-test, $U = 2.402$, $p < 0.0001$. Scale bars: **a, c, e** 500 µm, **g,** on millimetre paper. * = $p < 0.05$, ** = $p < 0.01$, *** = $p < 0.001$. **** = $p < 0.0001$

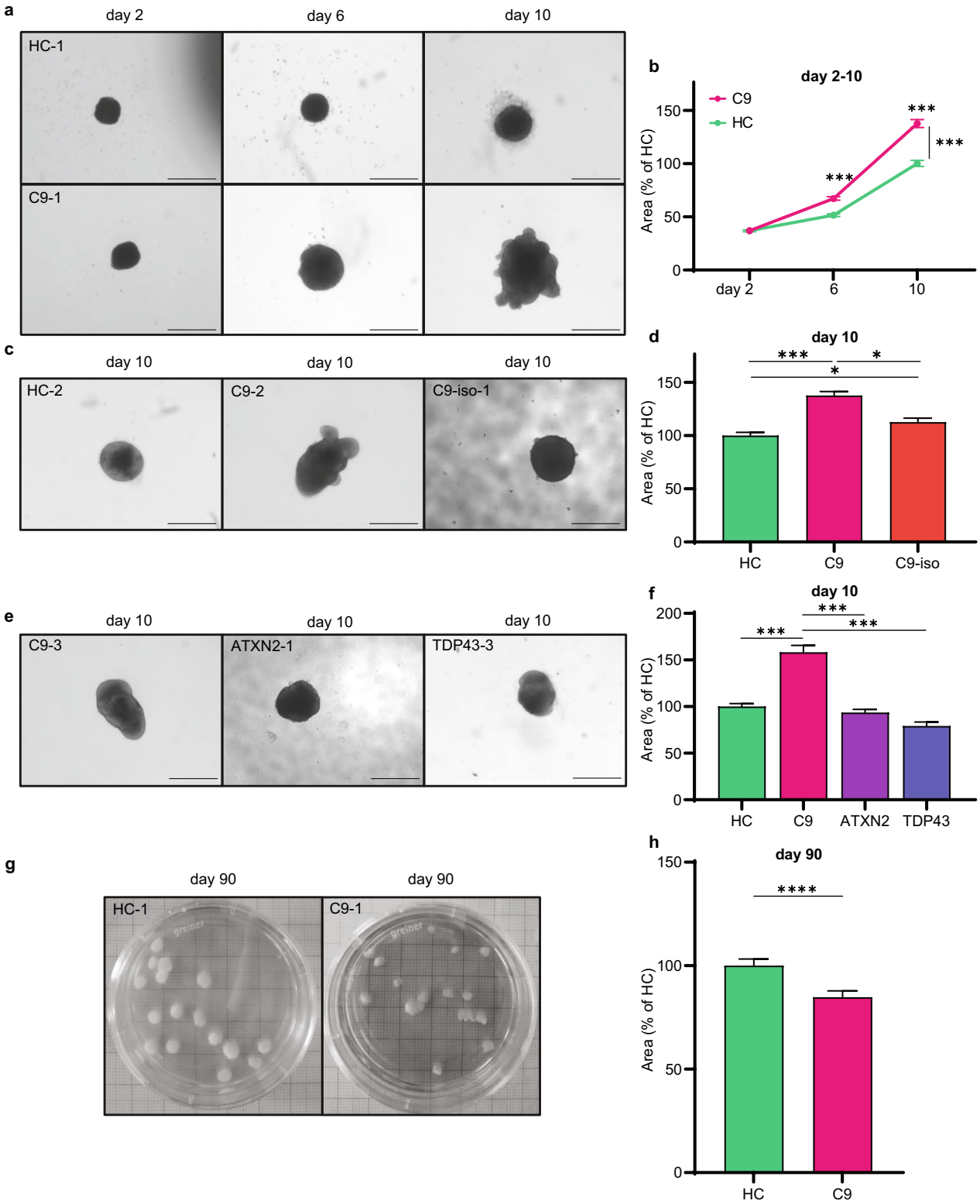

Fig. 2 (See legend on previous page.)

but not C9-iso, organoids (Fig. 4c, One-way ANOVA, Holm–Sidak's multiple comparisons test, $F(2,42)=4.389$, $p=0.019$; HC-C9: $p_{adj}=0.04$, C9-C9-iso: $p_{adj}=0.02$). In addition to CTIP2$^+$ neurons, radial glia cells were examined using immunohistochemistry for SOX2. ScRNA-seq analysis revealed changes in radial glia populations (Fig. 3g) and KI67 immunostaining hinted at changes in the organization of radial glia cells in VLZ (Fig. 1c). In day 90 HC organoids, most SOX2$^+$ radial glia resided in the VLZs and only a few were found in the MAP2$^+$ neuronal region. In contrast, in C9 organoids SOX2 labelling of the VLZ was more diffuse and many SOX2$^+$ cells were found in MAP2$^+$ parts of the organoid (Fig. 4d, Supplementary Fig. 4a). To further examine the VLZ in C9 organoids, whole-mount immunostaining of day 90 organoids was performed for ZO-1 (end feet marker RGC) and SOX2 (nuclear marker RGC), to mark lumen and VLZ structures, followed by tissue clearing and fluorescent light sheet microscopy (FLSM; Supplementary Fig. 4b). This revealed a decrease in the total volume of SOX2$^+$ VLZ structures and in the size of individual SOX2$^+$ VLZ structures in C9 versus HC organoids (Fig. 4e, Supplementary Fig. 4c–e).

In all, these data show that C9-HRE leads to a reduction of CTIP2$^+$ deep layer neurons and an abnormal organization of SOX2$^+$ radial glia cells.

Changes in the pre-synapse and synaptic proteins in C9-ALS/FTD

In addition to changes in deep layer neurons and radial glia, our analysis revealed cell type-specific gene expression changes, including reduced expression of different glutamatergic synaptic genes in different neuronal clusters (Fig. 3, 5a). This is in line with observations in human *post-mortem* tissue and animal models [24, 27]. However, the development of these changes and their functional consequences in complex human brain tissue remain largely unknown. The cellular and structural complexity of neural organoid models, which resembles the multicellular human brain environment and promotes neuronal maturation, provide a unique tool for further dissecting these C9-ALS/FTD-associated phenotypes. Therefore, glutamatergic synapses were visualized using immunostaining for synaptophysin (SYP) and SHANK2 to label the pre- and post-synapse, respectively, in organoid sections. MAP2 served as a marker for neuronal dendrites. *SHANK2* but not *SYP* expression was decreased in the scRNA-seq data (Supplementary Table 3). Analysis of SHANK2 and SYP expression revealed numerous synaptic structures and abundant co-localization in day 90 HC and C9 organoids (Supplementary Fig. 5a). Automated quantification revealed fewer SYP (Unpaired t-test, $t(66)=4.275$, $p<0.0001$), but not SHANK2 puncta (Mann–Whitney t-test, $U=452$, $p=0.1816$), in C9 as compared to HC organoids (Fig. 5b). Colocalization was reduced in C9 samples, but this effect was not statistically significant (Fig. 5c; Mann–Whitney t-test, $U=449$, $p=0.1687$). Further, SYP puncta were approximately 10% smaller in size in C9 as compared to HC organoids (Fig. 5d; Unpaired t-test, $t(66)=3.469$, $p=0.0009$) and the frequency of smaller puncta was higher in C9. SHANK2 puncta size was similar between conditions (Supplementary Fig. 5b; Unpaired t-test, $t(66)=0.2443$, $p=0.8078$). Next, the signal intensity of puncta was measured as a readout of protein expression at synaptic terminals. The intensity of the SYP puncta was ~12% reduced in C9 organoids (Fig. 5e; Unpaired t-test, $t(66)=2.456$, $p=0.0167$), while the intensity of SHANK2 puncta was unchanged (Fig. 5e; Unpaired t-test, $t(66)=0.4488$, $p=0.6551$). In addition to synaptic,

(See figure on next page.)

Fig. 3 Single-cell RNA sequencing of day 90 control and C9-ALS/FTD cerebral organoids. **a** Schematic representation of the single-cell RNA sequencing (scRNA-seq) approach. Day 90 organoids from healthy control (HC; HC-1, HC-2 and HC-3) and C9-ALS/FTD (C9-ALS-1, C9-ALS-2, C9-ALS-4) were dissociated, sequenced using a 10X Genomics platform, and analysed. N = 8 organoids per line were used. After quality control, 21.113 cells were detected which expressed 31.989 genes. **b** Uniform manifold approximation and projection (UMAP) plot of the filtered and normalized scRNAseq data showing 28 color-coded clusters as detected by the Leiden algorithm. **c** UMAP plot showing the RNA-seq data color-coded by disease condition. **d** Seventeen cell types were identified in day 90 cerebral organoids regardless of disease condition. Cell types are shown in a color-coded UMAP plot and a dendrogram. Clusters that belonged to the same cell type were grouped, e.g. radial glia 1 and 2. One C9 sample contained retinal pigment epithelial cells, which were omitted from the analysis. **e** UMAP plot showing expression of marker genes for the annotated cell types; *MAP2*—neural soma and dendrites; *TUBB3*—neuronal cytoskeleton; *BCL11B (CTIP2)*—deep layer neurons; *GAD1*—GABAergic neurons; *SHANK2*—postsynapse; *SYP*—presynapses; *GRIA1 (GluR1)*—postsynapse; *FABP7 (BLBP)*—radial glia. **f** Dot plot showing the scaled and normalized expression of 1–3 genes per annotated cluster on left side. The genes were selected from literature to mark specific cell types as indicated on the top row. Number of cells per cell type is indicated on the right. **g** Cell type composition analysis of the scRNA-seq data. Number of cells per cell type relative to total cell number for C9 and HC. Cell types are ordered by percentual change between conditions. Cell type colors are the same as in **d**. **h** Differentially expressed genes (DEGs) in C9 (as compared to HC) organoids within each cell type were analyzed using KEGG pathway analysis. Size of the circle represents the number of cell type comparisons where this pathway was significantly altered. For a full overview of DEGs and KEGG pathway results, see Supplementary Table 3 and 4. ULN, (upper layer) neuron; gliogenic, non-neuronal2; RG/eN, radial glia/early neuron; astrocyte, glia/astrocyte

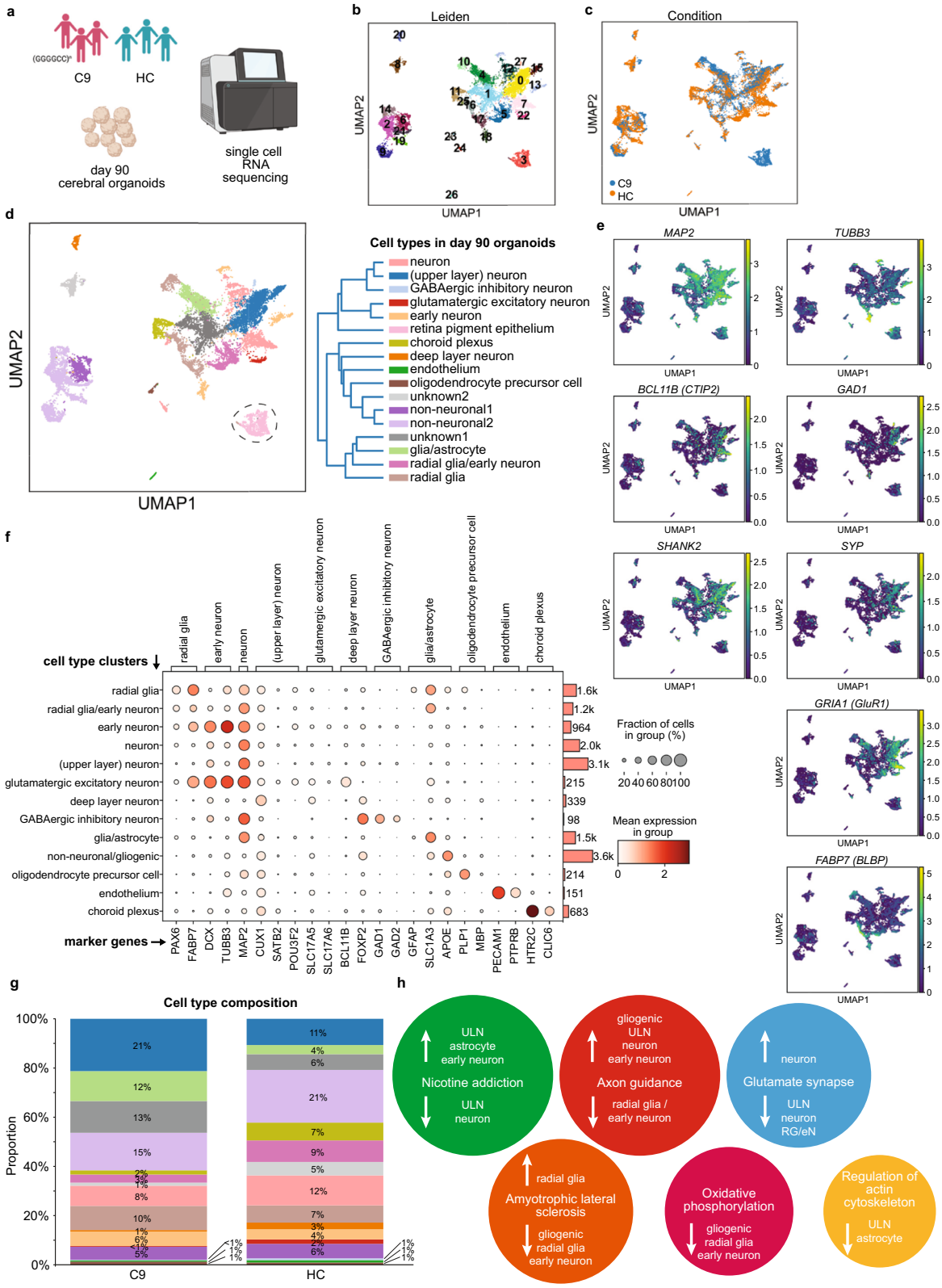

Fig. 3 (See legend on previous page.)

non-synaptic expression of SYP and SHANK2 in MAP2$^+$ dendrites outside the puncta was quantified (Supplementary Fig. 5c). This revealed a 30% decrease in the dendritic expression of both SYP and SHANK2 (Fig. 5f; Unpaired t-test, SYP: $t(66)=2.519$, $p=0.0142$; SHANK2: $t(66)=3.221$, $p=0.0020$), in line with overall reduced expression in the scRNAseq-data. Finally, a larger set of glutamatergic synaptic genes was studied by qPCR in day 90 HC and C9 organoids. Candidates included genes downregulated in the scRNAseq data (Fig. 5a) and genes coding for a few major synaptic components (Synapsins (*SYN2* and *SYN3*), Bassoon (*BSN*), and *PSD95*). The expression of 8 genes was significantly reduced in C9 as compared to HC organoids, while expression of *PSD95* was not different between C9 and HC (Fig. 5g–k, Supplementary Fig. 5d–g, Mann–Whitney two-tailed t-test, *BSN*: $U(19)=0$, $p<0.0001$; *EAAT2*: $U(19)=7$, $p=0.0005$; *PSD95*: $U(18)=25$, $p=0.1288$; *SLC17A7* (vGlut1): $U(17)=0$, $p<0.0001$; *SYN2*: $U(19)=7$, $p=0.0005$).

Together, these data unveil prominent pre-synaptic changes and reduced expression or altered distribution of several pre- and post-synaptic proteins and mRNA transcripts in C9 organoids.

Reduced synaptic transmission in C9-ALS/FTD cerebral organoids

Cerebral organoids have been shown to contain electrophysiologically active neuronal networks [61, 62, 95]. Therefore, to assess whether the observed changes at the pre-synapse and in the expression or distribution of different synaptic proteins lead to changes in synaptic transmission and neuronal function, we adapted a cerebral organoid slice model [44] for electrophysiological patch-clamp experiments. This for the first allowed high-resolution analysis of synaptic connectivity of C9 neurons in three-dimensional human brain tissue. Organoids were sliced at day 55 and measured between day 90 and 120 (Fig. 6a). Per line, 5 slices were obtained from 4 organoids which were cultured in a trans-well system. Cells were filled with biocytin afterwards to verify that recorded cells were neurons (Fig. 6b). Electrophysiological comparison of neurons in C9 and HC organoids did not detect differences in passive membrane properties (Fig. 6c–e; Unpaired two-tailed t-tests, c) Analysis of series resistance (Rs). $t(49)=0.4167$, $p=0.6787$. d) Analysis of membrane resistance (Rm). $t(49)=0.8120$, $p=0.4207$. e) Analysis of membrane capacitance (Cm). $t(49)=1.382$, $p=0.1733$)). However, resting membrane potential was significantly depolarized in C9 neurons, which suggests decreased synaptic maturity (Fig. 6f; $t(46)=2.543$, $p=0.0144$). Further, the frequency of spontaneous excitatory post synaptic currents (sEPSCs) was decreased in C9 neurons, while sEPSC amplitude was unchanged (Fig. 6g, h; $t(26)=2.623$, $p=0.0144$ and $t(26)=0.1069$, $p=0.9157$). Not all recorded cells displayed sEPSCs, but the percentages of this occurrence did not differ between HC and C9 (Fig. 6i; Chi-square test, $X^2(1)=0.235$, $p=0.628$). As sEPSC frequency reflects the level of synaptic connectivity in a neuronal network, these results suggest that C9 neurons are less well-connected. The percentage of neurons in which action potentials (AP) could be evoked was lower in C9 as compared to HC (Fig. 6j; Chi-square test, $X^2(1)=0.7212$, $p=0.3958$), but this effect did not reach statistical significance. A similar trend was observed for repetitive APs (Fig. 6k; Chi-square test, $X^2(1)=0.4898$, $p=0.4840$). Spontaneous action potentials occurred at a similar frequency in C9 and HC neurons (Fig. 6l; Chi-square test, $X^2(1)=0.01959$, $p=0.8887$).

Together, these data suggest reduced synaptic transmission and neuronal activity in C9 cerebral organoids that may reflect the concomitant structural synaptic changes and alterations in synaptic protein expression and distribution.

Presymptomatic carrier organoids show C9-HRE pathology and various molecular and cellular phenotypes

Presymptomatic C9-HRE carriers show robust structural changes in the brain [31, 52, 69, 73, 97, 119]. To explore

(See figure on next page.)

Fig. 4 C9-HRE causes a reduction of deep layer neurons and disorganized radial glia. **a** Immunohistochemistry for CTIP2, to mark deep layer neurons (red), and MAP2, to label neuronal regions (green), in day 90 healthy control (HC), C9-ALS/FTD (C9) and corresponding isogenic control (C9-iso) organoids. Dotted line indicates the border of ventricular-like zones (VLZ). DAPI in blue. **b, c** Quantitative PCR for the deep layer neuron marker *CTIP2* in day 90 HC and C9 organoids (**b**) and day 45 HC, C9, and C9-iso (**c**) organoids. Expression is normalized to *TBP* and *RPII*. Graphs show mean ± SEM, symbols indicate specific lines and dots represent an average measurement of 3 organoids pooled per independent organoid induction (**b**: n = 4 C9, and n = 3 HC, Mann–Whitney t-test, $U=7$, $p=0.0005$; **c**: n = 3 HC, n = 4 C9 and n = 3 C9-iso, One-way ANOVA, Holm–Sidak's multiple comparisons test, $F(2,42)=4.389$, $p=0.019$). **d** Immunohistochemistry for CTIP2, to mark deep layer neurons (red), MAP2, to label neuronal regions (green), and SOX2, to mark neural stem cells in the VLZ (light blue) in day 90 HC, and C9organoids. Dotted line indicates the border of VLZs. DAPI in blue. **e** Whole-organoid immunostaining followed by 3DISCO tissue clearing and fluorescent lightsheet imaging. Representative 3D rendering of an HC and C9 organoid, in which the tight junction marker ZO-1 depicts the borders of the ventricular lumen in red and the nuclear marker TOPRO3 indicates the denser ventricular-like zones (VLZs) in green, which was confirmed by the stem cell marker SOX2 in another channel. The selection volume of the VLZs is shown in yellow. Scale bars: **a** 50 µm, **d** 150 µm, **e** 100 µm * = $p<0.05$, *** = $p<0.001$

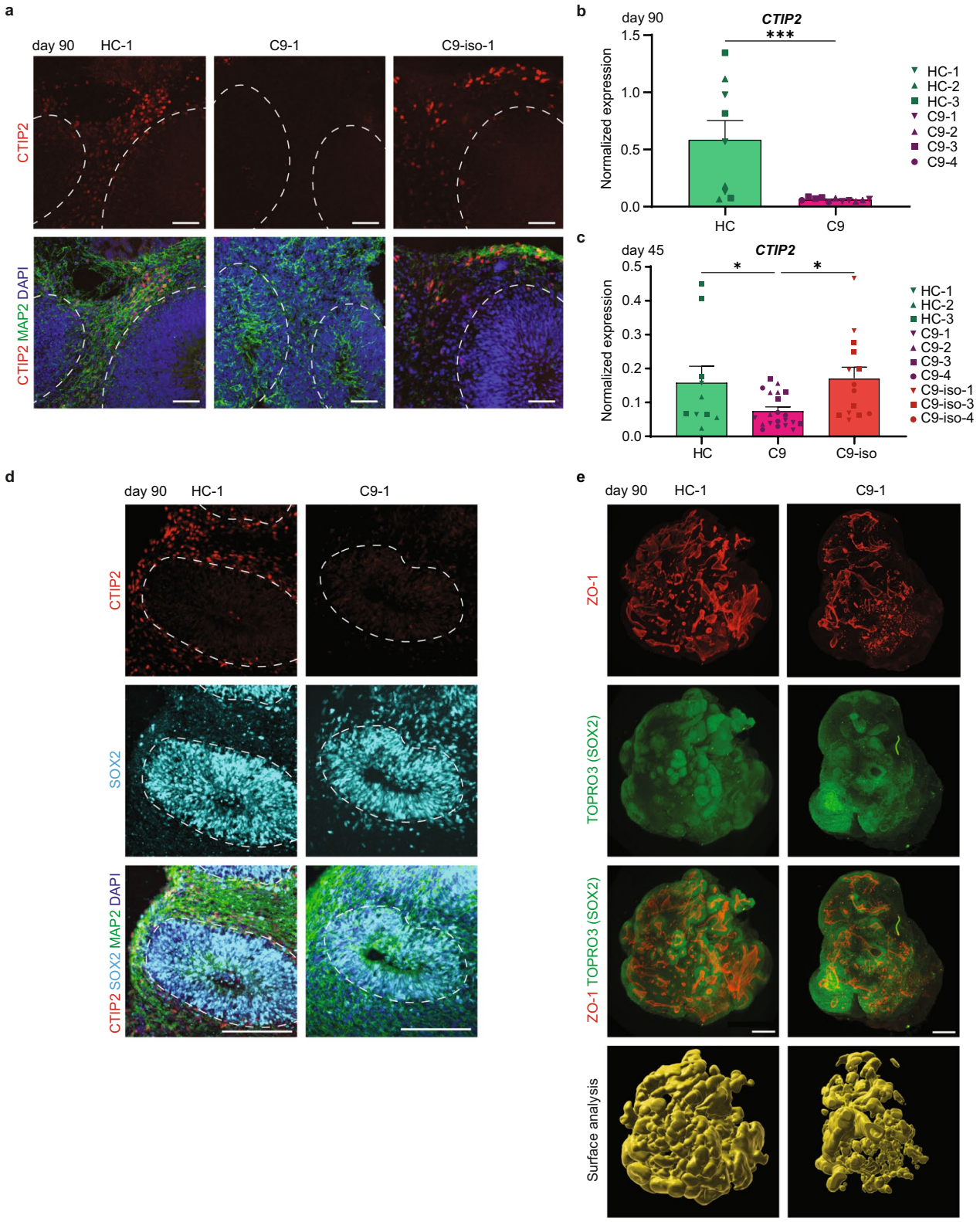

Fig. 4 (See legend on previous page.)

whether cerebral organoids can help dissect underlying presymptomatic disease mechanisms or act as a platform for (personalized) therapy development, we next generated iPSC-derived cerebral organoids from four family members of C9-ALS/FTD patients who carry C9-HRE but did not display symptoms at the time of skin biopsy (termed C9-carriers; Supplementary Fig. 6a-h). HRE were detected on one allele in C9-carrier iPSCs with a median length between 666–998 repeats (Fig. 7a). Similar to HC and C9 organoids, C9-carrier organoids displayed VLZs and MAP2$^+$ neural regions and comparable levels of *TUBB3* and *DCX* at day 90 (Fig. 7b, c; One-way ANOVA, *TUBB3*: $F(2,20)=4.929$, $p=0.081$; *DCX*: $F(2,20)=5.349$, $p=0.0626$). Western blot analysis showed a ~25% reduction in C9ORF72 expression in C9-carrier organoids compared to HC (Fig. 7d; One-tailed t-test, $t(10)=1.521$, $p=0.0796$). Further, MSD-ELISA assays confirmed the presence of poly(GA) and poly(GP) at day 90 (Fig. 7e). Interestingly, levels of poly(GA), but not poly(GP), were higher in C9 as compared to C9-carrier organoids. Finally, sense RNA foci were observed in the nucleus of some, but not all, cells of day 90 C9-carrier organoids (Fig. 7f, Supplementary Fig. 7a). In all, these results for the first time show that cerebral organoids derived from presymptomatic C9-HRE carriers display extensive C9-HRE molecular pathology.

Next, we investigated whether organoids derived from presymptomatic C9-carriers display phenotypes as observed in C9 organoids. C9-carrier organoids were subjected to a selection of analyses performed on C9-organoids (Fig. 1, 2, 3, 4, 5, 6) to cover a range of molecular and cellular phenotypes at early (up to day 10) and later developmental stages (day 45 and 90) (i.e. organoid size, CTIP2 and SOX2 distribution, and synaptic gene expression). Interestingly, size analysis of early C9-carrier organoids revealed an increased area as compared to HC at day 10 (Fig. 8a–c, One-way ANOVA – Kruskal–Wallis test with Dunn's correction for multiple testing, $F(5,267)=98.12$, $p<0.0001$; Supplementary Fig. 8a). However, further analysis showed that organoids of (1) C9-carrier-3 and -4 were significantly larger ($p_{adj}<0.0001$ and 0.0030) than HC, (2) C9-carrier-2 showed a trend to be larger ($p_{adj}=0.0511$), and (3) C9-carrier-1 were not different from HC ($p_{adj}=0.5376$). In general, C9-carrier organoids were much smaller than C9 organoids (Fig. 8b, c). Size analysis at day 90 showed that part of the C9-carrier organoids were also significantly smaller than HC, as observed for C9 organoids (Figs. 2g–h, 8d, one-way ANOVA—Kruskal–Wallis test, $F(5,413)=58.49$, $p<0.001$; Supplementary Fig. 8b). Interestingly, while C9-carrier-2 and -4 organoids were smaller ($p_{adj}<0.001$ and <0.001), C9-carrier-1 and -3 organoids were more similar to HC ($p_{adj}=0.330$ and >0.999). Together, these results reveal size phenotypes in C9-carrier organoids.

Our analysis of C9 organoids also showed a reduction in *CTIP2* mRNA expression and the number of CTIP2$^+$ deep layer neurons together with an abnormal organization of SOX2$^+$ radial glia cells (Fig. 4). qPCR and immunohistochemistry revealed that although *CTIP2* expression was generally decreased in C9-carrier organoids ($p_{adj}<0.001$) as compared to HC (Fig. 8e, one-way ANOVA, Tukey's multiple comparisons test, $F(2,34)=13.91$, $p<0.001$), only some lines (C9-carrier-3 and -4) but not others (C9-carrier-1 and -2) displayed a reduction in CTIP2$^+$ neuron number at day 90 using

(See figure on next page.)

Fig. 5 Pre- and post-synaptic changes in the expression and distribution of synaptic proteins and mRNA transcripts. **a** Schematic overview of the pre- and postsynaptic compartment showing differentially expressed genes (DEGs) related to 'glutamatergic synapse' and reduced in C9-ALS/FTD (C9) neurons (in red) in the scRNA-seq dataset of day 90 healthy control (HC) and C9 organoids. **b** Quantification of the relative number of SYP and SHANK2 puncta. Graphs show mean, dots represent puncta normalized to the MAP2$^+$ area of one image, and images were taken of three organoids from 2–3 independent differentiations (n = 3 HC, n = 4 C9 lines). SYP: Unpaired two-tailed t-test, $t(66)=4.275$, $p=<0.0001$; SHANK2: Mann–Whitney two-tailed t-test, $U=452$, $p=0.1816$. **c** Quantification of the colocalization of SYP and SHANK2 puncta. Graph shows mean, dots represent colocalization normalized to the MAP2$^+$ area of one image, images were taken of three organoids from 2–3 independent differentiations (n = 3 HC, n = 4 C9 lines). Mann–Whitney two-tailed t-test, $U=449$, $p=0.1687$. **d** Analysis of SYP puncta size averaged per image (left) or relative size frequency of individual puncta (right). Graph shows mean, dots represent average of one image, images were taken from three organoids from 2–3 independent differentiations (n = 3 HC, n = 4 C9 lines). Unpaired two-tailed t-test, $t(66)=3.469$, $p=0.0009$. **e** Quantification of the signal intensity of SYP and SHANK2 (SH2) in puncta. Graphs show mean, dots represent average of one image, and images were taken from three organoids from 2–3 independent differentiations (n = 3 HC, n = 4 C9). Unpaired two-tailed t-test, SYP: $t(66)=2.456$, $p=0.0167$; SHANK2: $t(66)=0.4488$, $p=0.6551$. **f** Quantification of the signal intensity of SYP and SHANK2 (SH2) in dendrites. Graphs show mean, dots represent average of one image, images were taken from three organoids from 2–3 independent differentiations (n = 3 HC, n = 4 C9). Unpaired two-tailed t-test, SYP: $t(66)=2.519$, $p=0.0142$; SHANK2: $t(66)=3.221$, $p=0.0020$. **g–k** Quantitative PCR was performed for glutamatergic synaptic genes and major synaptic components in day 90 healthy control (HC) and C9-ALS/FTD (C9) organoids. Expression was normalized to the housekeeping genes *TBP* and *RPII*. Graphs show mean ± SEM, symbols indicate the cell lines, dots represent an average measurement of 3 organoids pooled per independent organoid induction (n = 4 C9, and n = 3 HC lines). Mann–Whitney two-tailed t-test, *BSN*: $U(19)=0$, $p<0.0001$; *EAAT2*: $U(19)=7$, $p=0.0005$; *PSD95*: $U(18)=25$, $p=0.1288$; *SLC17A7* (vGlut1): $U(17)=0$, $p<0.0001$; *SYN2*: $U(19)=7$, $p=0.0005$. Additional genes are displayed in Supplementary Fig. 5d-g. Scale bar: **b** 40 µm. * = $p<0.05$, ** = $p<0.01$, *** = $p<0.001$, **** = $p<0.0001$

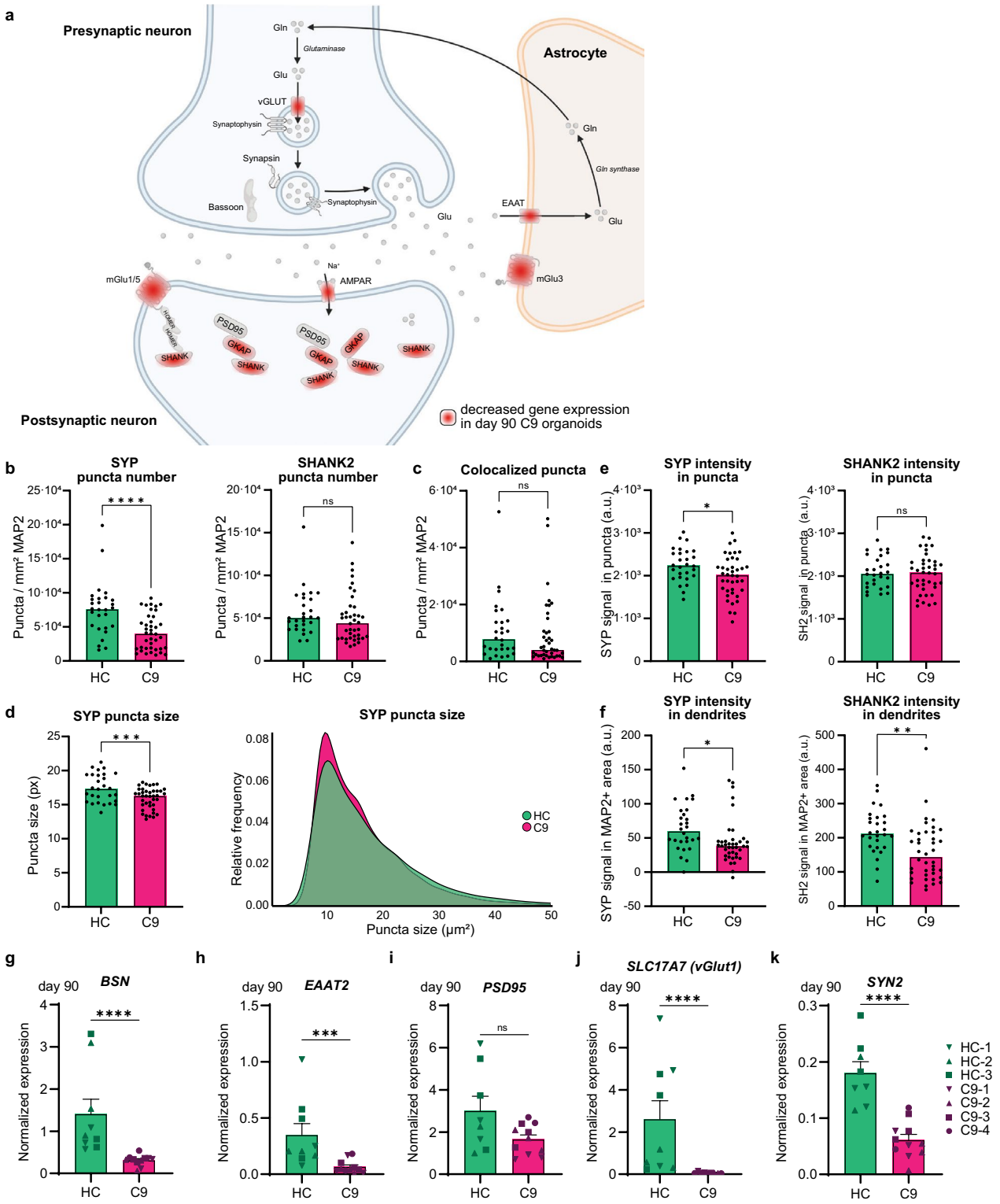

Fig. 5 (See legend on previous page.)

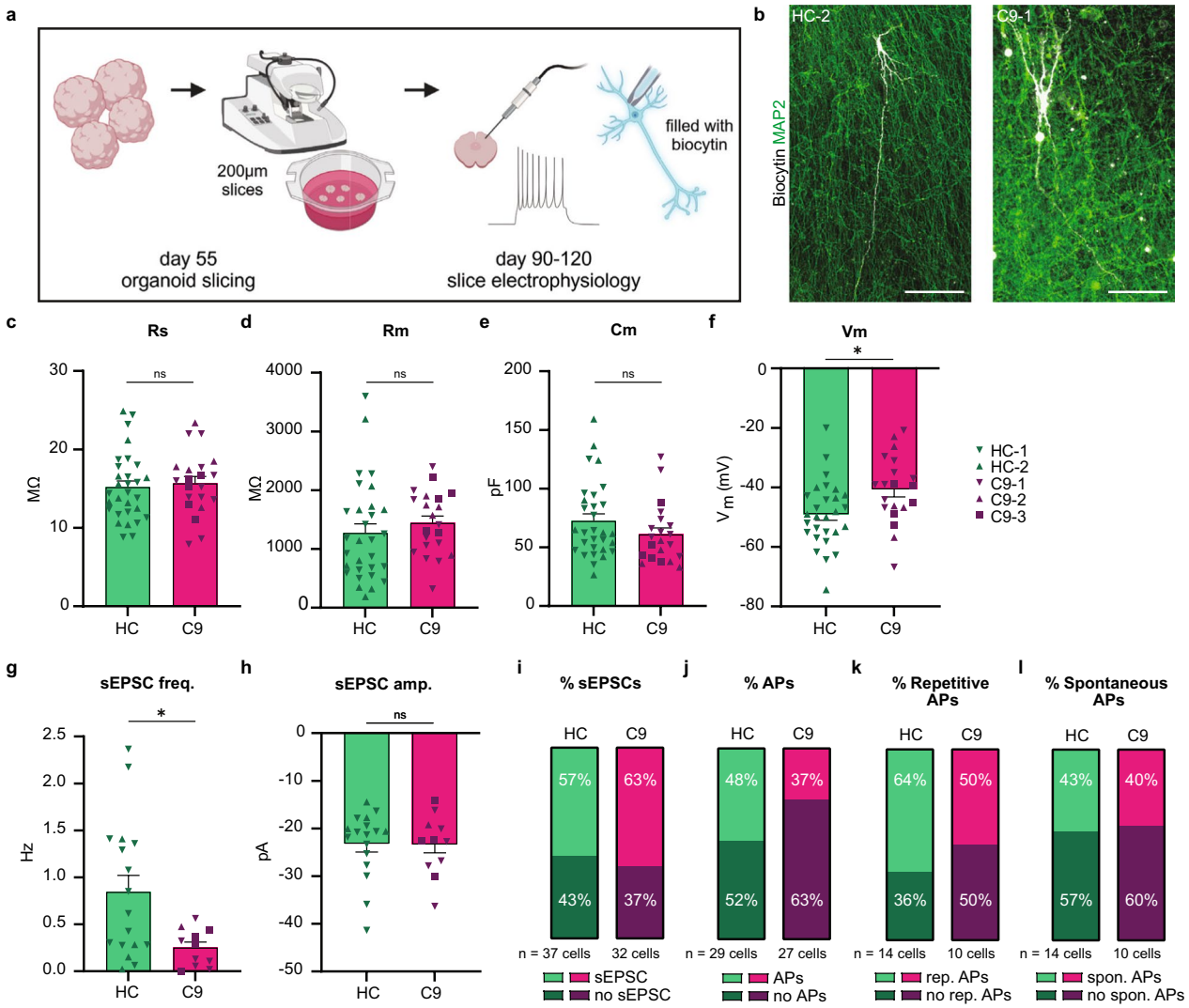

Fig. 6 Changes in synaptic and neuronal activity in C9-ALS/FTD cerebral organoids. **a** Schematic of organoid slicing and the electrophysiological set-up. **b** Representative image of immunohistochemistry on organoid slices after electrophysiological measurements showing biocytin-filled neurons (white) embedded in a MAP2$^+$ dendritic network. HC, healthy control; C9, C9-ALS/FTD. **c**–**h** Electrophysiological analysis. Graph shows mean ± SEM, dots represent individual cells from 4 organoids with 5 slices each from 1 organoid differentiation per iPSC line (n = 2 healthy control (HC), n = 3 C9-ALS/FTD (C9) lines). Unpaired two-tailed t-tests, **c** Analysis of series resistance (Rs). $t(49) = 0.4167$, $p = 0.6787$. **d** Analysis of membrane resistance (Rm). $t(49) = 0.8120$, $p = 0.4207$. **e** Analysis of membrane capacitance (Cm). $t(49) = 1.382$, $p = 0.1733$. **f** Resting membrane potential (Vm). $t(46) = 2.543$, $p = 0.0144$. **g** Spontaneous excitatory post synaptic current (sEPSC) frequency. $t(26) = 2.623$, $p = 0.0144$. **h** sEPSC amplitude. $t(26) = 0.1069$, $p = 0.9157$. **i**–**l** Percentage of cells in which sEPSCs, action potentials (APs), repetitive APs or spontaneous APs could be measured. Graphs show percentage of all cells. Cells from 4 organoids with 5 slices each from 1 organoid differentiation per iPSC line were measured (n = 2 HC, n = 3 C9 lines). **i** Percentage of cells with/without sEPSCs. Chi-square test, $X^2(1) = 0.235$, $p = 0.628$. **j** Percentage of cells in which APs could be elicited. Chi-square test, $X^2(1) = 0.7212$, $p = 0.3958$. **k** Percentage of cells with APs that displayed repetitive APs. Chi-square test, $X^2(1) = 0.4898$, $p = 0.4840$. **l** Percentage of cells with APs that showed spontaneous APs. Chi-square test, $X^2(1) = 0.01959$, $p = 0.8887$. Scale bar: **b** 100 µm. * = $p < 0.05$

immunohistochemistry. SOX2 labelling of the VLZ of C9-carrier organoids was more diffuse and many SOX2$^+$ cells were found in MAP2$^+$ parts of the organoid in all C9-carriers (Fig. 8f; Supplementary Fig. 8c).

Finally, we assessed synaptic gene expression in C9-carrier organoids. This experiment showed that the synaptic expression patterns of C9-carrier-2 and -4 were most similar to C9, while C9-carrier-1 behaved more similar to HC (Fig. 8g–m, Supplementary Fig. 8d-f; One-way ANOVA, Tukey's multiple comparisons test, *BSN*: $F(5, 34) = 6.186$, $p = 0.0004$; *EAAT2*: $F(5, 36) = 5.558$, $p = 0.0007$; *PSD95*: $F(5, 34) = 2.102$, $p = 0.0892$; *SHANK2*: $F(5, 35) = 6.840$, $p = 0.0002$; *SYN2*: $F(5, 35) = 6.644$, $p = 0.0002$; *SYN3*: $F(5, 35) = 6.800$, $p = 0.0002$).

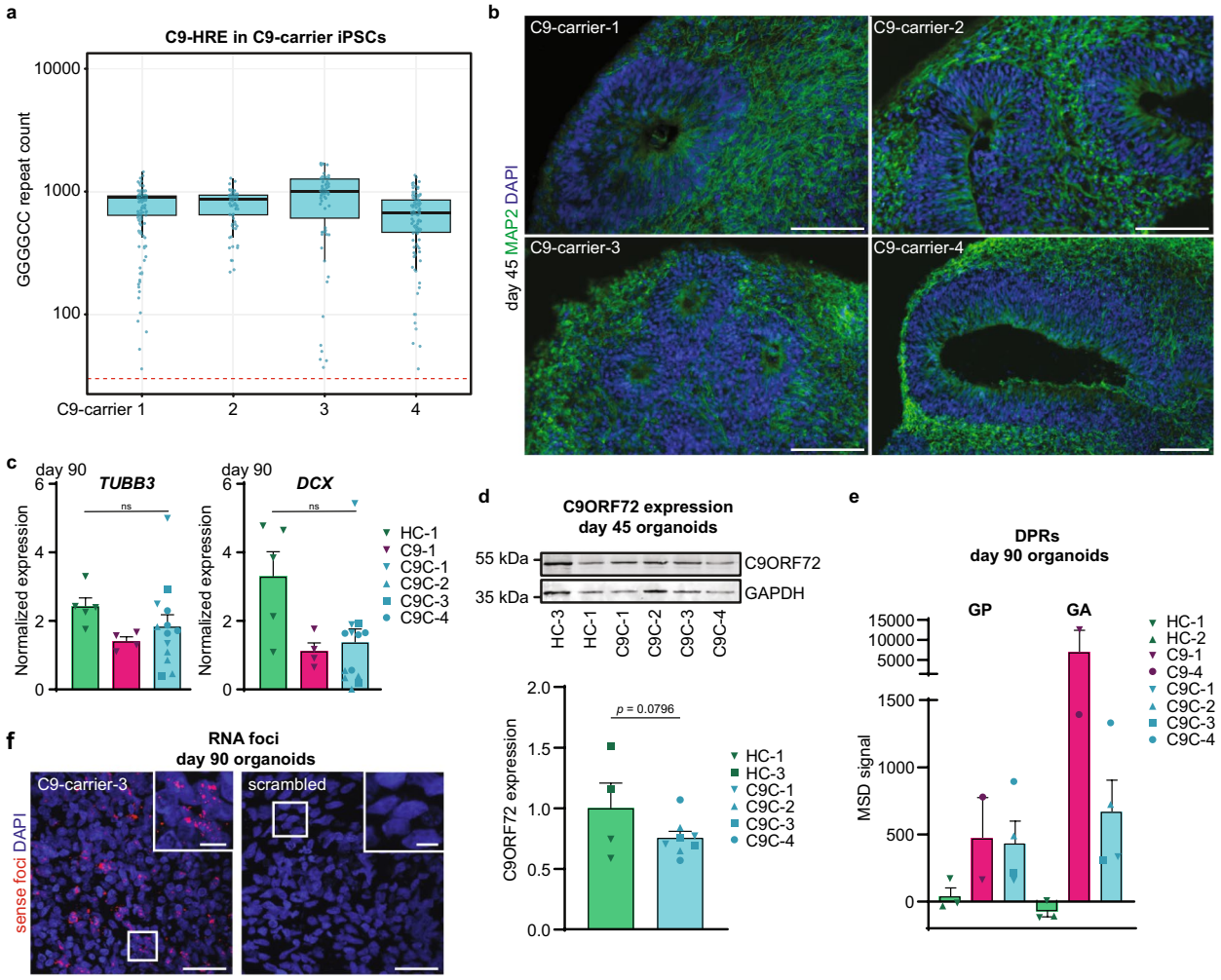

Fig. 7 Cerebral organoids from presymptomatic C9-HRE carriers show molecular pathology. **a** Nanopore sequencing of iPSCs from different *C9-HRE* carriers (C9-carrier-1–4, Supplementary Table 1) to determine GGGGCC repeat count. Dots represent individual reads, on which the box and whiskers plot is based. Red-dotted line indicates the 30-read cut-off used to separate the reads of the expanded and non-expanded allele. **b** Representative image of immunohistochemistry on cryosections of day 45 cerebral organoids from C9-carriers for MAP2 (green; neuronal part) in combination with DAPI to mark nuclei. **c** Quantitative PCR for the neuronal cytoskeleton marker *TUBB3* and early-born neuron marker *DCX* in day 90 healthy control (HC), C9-ALS/FTD (C9), and C9-carrier organoids. Expression is normalized to *TBP* and *RPII*. Data are shown as the mean ± SEM, symbols indicate specific lines and dots represent ≥ 3 pooled organoids. 2–5 independent organoid differentiations were performed per iPSC line, every data point is the average of two technical replicates. HC-1 and C9-1 were used as representative control and C9-ALS/FTD lines, respectively. One-way ANOVA, *TUBB3*: $F(2,20) = 4.929$, $p = 0.081$; *DCX*: $F(2,20) = 5.349$, $p = 0.0626$. **d** Example of Western blot analysis of C9ORF72 expression in day 45 HC and C9-carrier organoids. Graph shows mean ± SEM (normalized to GAPDH) and dots represent individual Western blot measurements of ≥ 3 organoids pooled per experiment. 2 Western blot replicates per line. 2 independent organoid differentiations were performed per iPSC line. One-tailed t-test, $t(10) = 1.521$, $p = 0.0796$. **e** Poly(GP) and poly(GA) levels were measured in day 90 organoids from HC, C9 and C9-carriers. Data are shown as the mean ± SEM and dots represent individual MSD measurements of ≥ 3 organoids pooled per experiment after background subtraction. **f** Representative images showing LNA-FISH for sense RNA foci (red) in cryosections of day 90 C9-carrier organoids. DAPI (blue) marks nuclei. Boxed areas are shown at higher magnification in the right upper corner (n = 4 C9-carrier lines). Scrambled control probes did not show signal (scrambled probe on C9-carrier-2 sample is displayed). Scale bars: **b** 100 µm, **f** 50 µm and 10 µm in higher magnification box

Together, these results show that several of the phenotypes observed in C9 organoids can also be found in presymptomatic C9-carrier organoids although the specific set of defects detected or their severity may vary, e.g. C9-carrier-4 appeared to phenotypically resemble C9, while C9-carrier-1 (a sibling of C9-carrier-4) organoids were more similar to HC (except for C9-HRE pathology and SOX2 misorganization).

Discussion

Human brain imaging and experimental studies indicate early changes in brain structure and connectivity in C9-ALS/FTD (C9) patients, even before symptom onset. Because these early disease phenotypes remain poorly understood, we derived and studied cerebral organoid models from (pre)symptomatic C9 patients. Our work revealed all three C9-HRE-related pathologies in cerebral organoids and novel opposite size differences at different stages of organoid development. Changes in cell type abundance and distribution were found at later stages, e.g. a reduction in the number of deep layer cortical neurons, together with synaptic deficits in excitatory neurons (Fig. 9a). Interestingly, organoids from presymptomatic C9-HRE carriers consistently showed C9ORF72 haploinsufficiency, DPRs and RNA foci. A selection of defects detected in C9 organoids was also observed in organoids from some, but not all, presymptomatic C9-HRE carriers. These results identify early C9-HRE-induced changes in cellular architecture and synaptic connectivity in complex brain tissue, show that in vitro models derived from presymptomatic *C9-HRE* carriers display extensive molecular pathology and cellular defects, and highlight the potential of cerebral organoids for defining initial disease phenotypes and developing therapeutic approaches, perhaps even at presymptomatic stages.

Molecular pathology and developmental changes in C9-ALS/FTD cerebral organoids

C9-HRE leads to reduced C9ORF72 expression and the generation of DPRs and nuclear RNA foci in C9 patients [7]. Thus far, poly(GA) DPRs have been reported in mature cerebral organoid slices [107]. Our current work confirms and extends these observations by detecting multiple distinct DPRs (poly(GA) and poly(GP)), and both C9ORF72 haploinsufficiency and sense RNA foci at earlier stages of organoid development. Our results are the first to show all three C9-HRE pathologies in cerebral organoids and align with recent work in C9 neuromuscular organoids [39].

Our analysis of C9 cerebral organoids identified opposite size differences at early and later stages of organoid development. At early stages (around day 10), C9 organoids were larger as compared to healthy and isogenic control organoids. These phenotypes were not not reported before and detected in organoids derived from other ALS genetic backgrounds (TDP-43-ALS, ATXN2-ALS). This indicates that increased organoid size is not a general ALS phenotype and resonates with the observation that the most prominent cortical changes are observed in C9 patients as compared to the general ALS patient population [11, 82]. It is, however, possible that ALS genetic backgrounds other than those tested here similarly affect organoid size. The early size defect was only partially rescued in isogenic control organoids, which hints at the involvement of additional mechanisms, e.g. additional genetic influences. How C9-HRE causes early accelerated organoid growth is unknown. Interestingly, re-expression of different cell cycle-associated proteins has been reported in C9 neurons [68, 87]. Cell cycle progression analysis did, however, not reveal differences between C9 and healthy control

(See figure on next page.)

Fig. 8 Presymptomatic C9-HRE carrier organoids varying degrees of molecular and cellular phenotypes. **a** Representative brightfield images of presymptomatic *C9-HRE* carrier (C9-carrier) organoids at day 2, 6 and 10. **b**–**c** Quantification of the cross-sectional area of HC, C9, and C9-carrier organoids at day 2, 6, and 10 (**b**) and at day 10 (**c**) based on images as in a. Size normalized to the HC average. Graphs show mean ± SEM, n = 12 organoids per timepoint times from 3 to 5 independent differentiations per iPSC line (n = 1 HC, n = 1 C9 n = 4 C9-carrier lines), one-way ANOVA—Kruskal–Wallis test with Dunn's correction for multiple testing, $F(5,267) = 98.12$, $p < 0.0001$. Trendlines in c represent average size of n = 3 HC (green) and n = 4 C9 (pink) as shown in Fig. 2d. **d** Quantification of the cross-sectional area of HC, C9, and C9-carrier at day 90 based on images as in Supplementary Fig. 8b. Size normalized to the HC average. Graphs show mean ± SEM, measurements from 3 to 6 independent differentiations per iPSC line, n = 1 HC, n = 1 C9, n = 4 C9-carrier lines, one-way ANOVA—Kruskal–Wallis test with Dunn's correction for multiple testing, $F(5,413) = 58.49$, $p < 0.001$. Trendlines indicate the average size of n = 3 HC (green) and n = 4 C9 (pink) as shown in Fig. 2h. **e** Quantitative PCR for the deep layer neuron marker *CTIP2* in day 90 HC, C9 and C9-carrier organoids. Expression is normalized to *TBP* and *RPII*. Graphs show mean ± SEM, symbols indicate specific lines and dots represent an average measurement of 3 organoids pooled per independent organoid induction, n = 3 HC, n = 4 C9 and n = 4 C9-carrier lines, One-way ANOVA, Tukey's multiple comparisons test, $F(2,34) = 13.91$, $p < 0.001$. Non-significant results are not displayed. **f** Immunohistochemistry for CTIP2, to mark deep layer neurons (red), MAP2, to label neuronal regions (green), and SOX2, to mark neural stem cells in the VLZ (light blue) in day 90 HC, C9 and C9-carrier organoids. Dotted line indicates the border of VLZs. DAPI in blue. **g–l** Quantitative PCR was performed for glutamatergic synaptic genes and major synaptic components in day 90 healthy control (HC), C9-ALS/FTD (C9), and C9-carrier organoids. Expression was normalized to the housekeeping genes *TBP* and *RPII*. Graphs show mean, dots represent an average measurement of 3 organoids pooled per independent organoid induction (n = 4 C9-carrier, n = 4 C9, and n = 3 HC lines). One-way ANOVA, Tukey's multiple comparisons test, *BSN*: $F(5, 34) = 6.186$, $p = 0.0004$; *EAAT2*: $F(5, 36) = 5.558$, $p = 0.0007$; *PSD95*: $F(5, 34) = 2.102$, $p = 0.0892$; *SHANK2*: $F(5, 35) = 6.840$, $p = 0.0002$; *SYN2*: $F(5, 35) = 6.644$, $p = 0.0002$; *SYN3*: $F(5, 35) = 6.800$, $p = 0.0002$. *DLGAP1*, *SLC17A7* (*vGlut1*), and *SYP* are displayed in Supplementary Fig. 8d–f. **m** Heatmap summarizing the results of the qPCR analysis of (glutamatergic) synaptic genes as in (**g**–**l**) relative to the highest expression detected for that gene. Asterisks mark significance of the group compared to HC. Test statistics are described in g–l. Scale bars: **a** 500 µm, **f** 150 µm. * = $p < 0.05$, ** = $p < 0.01$, *** = $p < 0.001$. **** = $p < 0.0001$

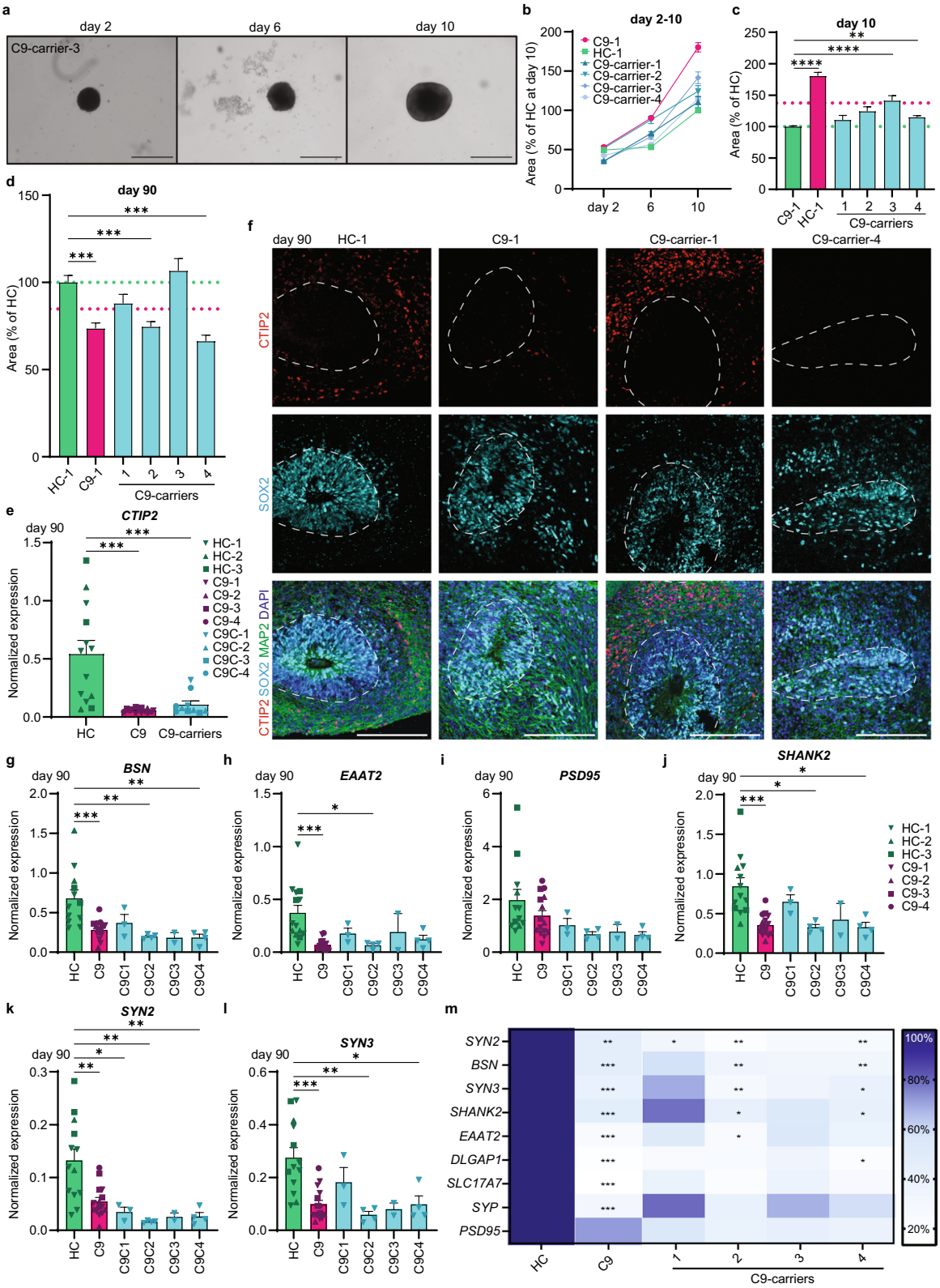

Fig. 8 (See legend on previous page.)

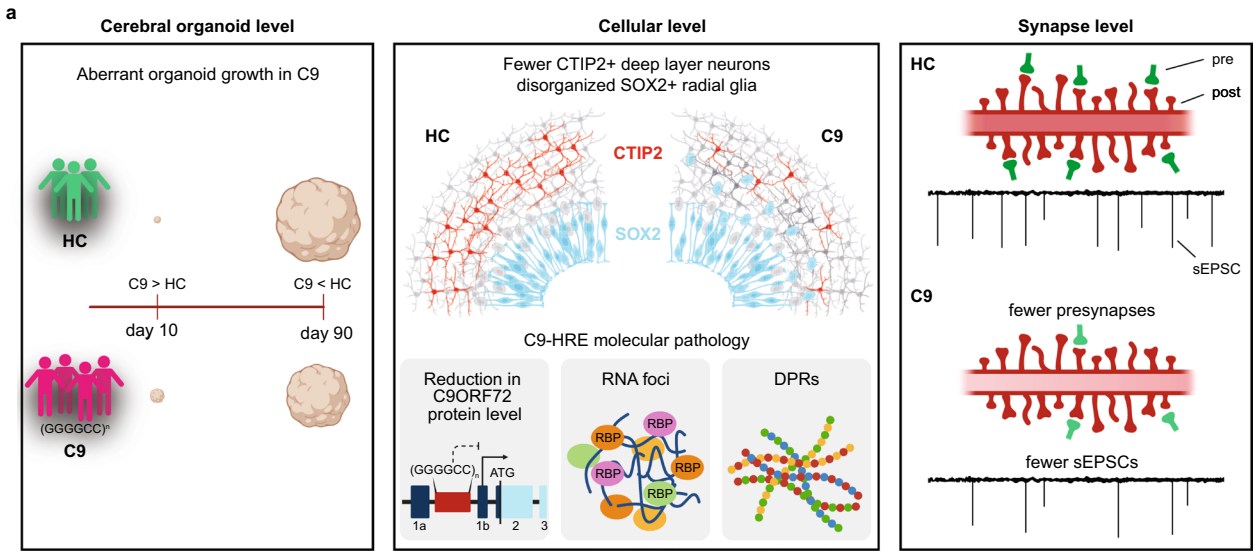

Fig. 9 Schematic overview of the findings of the study. **a** Graphical overview of the main findings of the study. At the level of whole organoids (left): C9 organoids were larger at day 10 and smaller at day 90, at the cellular level (middle): fewer CTIP2$^+$ deep layer neurons (red) and disorganized SOX2$^+$ radial glia (cyan) were detected. Moreover, C9 organoids displayed all three types of C9-HRE molecular pathology, and at the synapse level (right): fewer presynapses (green) and decreased expression of postsynaptic SHANK2 (red) in dendrites together with fewer spontaneous excitatory post-synaptic currents (sEPSCs; downward facing peaks)

(HC) iPSCs (Supplementary Fig. 9a; Two-way ANOVA, $F(2,114)=0.39$, $p=0.6787$). C9ORF72 has been implicated in different pathways that contribute to cell proliferation and differentiation, e.g. cytoskeletal control and intracellular trafficking [19, 104]. Some of these pathways were deregulated in our scRNA-seq data and constitute a valuable starting point for further studies into these early phenotypes.

Growth of the brain and of neural organoids depends in part on the initial symmetrical division of neuroepithelial cells followed by asymmetrical division of radial glia [10, 12, 46]. Early depletion of the stem cell pool could lead to initial accelerated development of neural tissue, followed by reduced growth at later stages. This mimics our phenotypic observations in early and later organoids. At day 90, the SOX2$^+$ neural stem cell pool area was reduced and SOX2$^+$ stem cells were dispersed in C9 organoids. Similar developmental changes in the organization of stem cells have been found in neural organoids modelling other, developmental, brain diseases [15, 74]. Whether the early and later effects on organoid size observed in our study are linked, and if not, how these later defects arise is unknown. Interestingly, DPR type-specific effects on stem cell proliferation have been reported. Whereas poly(AP) expression mostly affected PAX6$^+$ neural stem cells in 2D cultures, poly(GR) and poly(PR) inhibited KI67$^+$ dividing cells [48]. These observations support the exciting possibility that C9-HRE influences different stages of organoid development through distinct downstream pathological mechanisms.

Our scRNA-seq analysis of day 90 organoids revealed the presence of similar cell types in C9 and HC organoids. However, differences were detected in the abundance of specific cell types. For example, the number of CTIP2$^+$ deep layer cortical neurons, a vulnerable cell type in ALS/FTD, was reduced in C9 organoids, as confirmed by immunohistochemistry. No changes in cell type composition were recently reported in C9 cerebral organoid slices at later stages [107]. This apparent discrepancy may be explained by different factors, e.g. the number of lines analyzed (which was higher in our study), the model and timepoint of analysis, and markers used for confirmation (e.g. CTIP2 was not analyzed). No obvious increase in cell death was observed in C9 organoids (data not shown) [107] and we already detected changes in *CTIP2* expression at day 45. These observations together with the developmental nature of cerebral organoids at day 90 and previous mouse studies showing C9-HRE-induced neurodevelopmental effects [48] support a model in which C9-HRE cause developmental defects that affect specific cell populations, such as deep layer neurons. The accumulation of DNA damage and nuclear pyknosis in deep-layer neurons at later stages of organoid development [107], indicate that the changes found in our study are likely followed by more neurodegenerative changes in the same cell types.

Synaptic deficits in C9-ALS/FTD cerebral organoids

The presence of the same cell types in day 90 C9 and HC organoids provided an opportunity to assess cell type-specific gene expression changes and revealed changes in glutamatergic gene expression. This is in line with accumulating evidence of synaptic impairments in C9-ALS/FTD and upon C9 loss-of-function [27, 42]. C9ORF72 protein is present at pre- and postsynaptic terminals [6, 37, 123] and interacts with synaptic proteins such as SYP [9]. C9ORF72 deficiency and/or C9-HRE result in decreased expression of synaptic proteins and a reduced number of excitatory synapses in vitro, in different animal models in vivo and in post-mortem brain tissue [9, 21, 36, 49, 50, 59, 73, 106]. Our work complements these observations by identifying prominent changes in synaptic gene expression in excitatory neurons, structural presynaptic changes, and altered synaptic and dendritic expression of pre- and postsynaptic proteins in patient-derived 3D brain tissue models. Further, our approach, for the first time, allowed detailed electrophysiological assessment of synaptic and neuronal function in a multi-cellular and complex tissue carrying C9-HRE. Previous studies have reported hyperexcitability [20, 30, 43, 85], or hypoexcitability phenotypes [1, 9, 26, 30, 98], or lack of differences [38, 101, 107] in neuronal cultures. The significantly depolarized resting membrane potential observed in C9 organoids (Fig. 6f) is in line with reports of hyperexcitability. Our results in 3D organoids indicate reduced synaptic and neuronal function at 90 days of culture. Further studies are needed to establish whether this, likely developmental, phenotype persists in more mature organoid cultures. This is, for example, important as the maturation of astrocytes, essential for synaptic function, only commences around day 70 in cerebral organoids [115]. Furthermore, synaptic defects in C9 cultures have been reported to be culture age-dependent [24, 105]. The precise mechanism by which C9-HRE causes different synaptic phenotypes is incompletely understood, but the reported role of C9ORF72 in intracellular trafficking, also at synapses [19], is in line with our observation of reduced presynaptic and dendritic expression of proteins such as SYP and SHANK2.

In all, our results reveal widespread synaptic changes in C9 cerebral organoids, and both complement and strengthen previous work identifying synaptic changes as early and convergent pathogenic events. While a large body of work has focused on postsynaptic changes [42], our work and that of others [27] highlights the central (pre)synapse as a crucial structure in C9-ALS/FTD. Human PET imaging studies have revealed reduced synaptic density in the thalamus of presymptomatic cases [73]. Although we did not perform an exhaustive synaptic analysis of C9-carrier organoids, our synaptic gene expression data align with these findings by highlighting early changes in synaptic genes. Our data support the idea that neural organoids constitute a valuable additional tool for further unveiling the synaptic phenotypes underlying C9-ALS/FTD and other neurodegenerative diseases.

C9-HRE pathology and disease phenotypes in organoids from presymptomatic carriers

Presymptomatic C9-HRE carriers display several but not all phenotypes found in C9-ALS/FTD cases [31, 52, 69, 73, 97, 119]. Further, the penetrance of the C9-HRE is incomplete and age of onset varies from 40 to 90 years of age [81, 121]. It is therefore difficult to predict if or when C9-HRE carriers will display their first clinical symptoms. To explore whether cerebral organoids may help to predict symptom onset and the dissection of presymptomatic disease mechanisms, we generated cerebral organoids from presymptomatic C9-HRE carriers. Interestingly, all three C9-HRE pathologies were detected in organoids from all four C9-carriers. This is in line with studies detecting C9-HRE pathology in brain tissue before symptom onset [88, 112]. Based on these observations one could argue that the mere presence of C9-HRE in C9-carrier organoids will be sufficient to induce C9-HRE pathology and downstream phenotypes as found in C9 organoids. In contrast, our analysis identified a lack of most phenotypes in one C9-carrier (C9-carrier-1, except for changes in $SOX2^+$ cell distribution) but detected a full range of defects in a presymptomatic sibling (C9-carrier-4). Two other unrelated C9-carriers displayed distinct sets of cellular phenotypes. One limitation of our study is that we do not yet know if or when these C9-carriers will display their first symptoms. The difference in phenotypes (or lack thereof) could simply reflect time left until disease onset. Alternatively, these differences could be caused by other factors such as additional polygenic risk related to the idea that ALS is a multistep process [2]. This is in line with recent work suggesting that even in C9-ALS/FTD pedigrees, genetic factors other than C9-HRE may contribute to the disease process [94]. Our observations show that the presence of C9-HRE pathology is not indicative of the presence of other cellular phenotypes, at least in vitro. We, however, found that poly(GA) levels were higher in C9 as compared to C9-carrier organoids. It is therefore possible that in depth quantification of C9-HRE pathologies, and perhaps other markers such as TDP-43 localization or Nf-L levels, will improve correlation with the development of pathogenic events. If proven, such quantitative measurements could feed into multi-modal prediction platforms that include other patient data, such as brain imaging and functional assessments, for improved diagnosis and prognosis.

In conclusion, by exploiting the potential of human neural organoid models we identify early changes in cell type abundance, developmental processes, and synaptic

dysfunction that resonate with early changes in brain structure and connectivity observed in C9-ALS-FTD patients in vivo. Analysis of organoids from presymptomatic C9-HRE carriers consistently revealed all three C9-HRE pathologies and showed C9-carrier-specific expression of the cellular phenotypes that are consistently observed in C9-ALS/FTD organoids. Overall, our observations support the notion that the cellular and structural complexity of 3D neural organoids, which resembles the multicellular environment of the human brain and promotes neuronal maturation, provides a valuable tool for the molecular, cellular, and functional interrogation of ALS pathogenesis and a platform for (personalized) therapy development.

Abbreviations

ALS	Amyotrophic lateral sclerosis
AP	Action potential
ATXN2-ALS	ALS line carrying an intermediate repeat expansion in Ataxin 2
C9	C9ORF72
Cm	Membrane capacitance
DPR	Dipeptide-repeat protein
FLSM	Fluorescent light sheet microscopy
FTD	Frontotemporal dementia
HC	Healthy control
HRE	Hexanucleotide repeat expansion
iPSC	Induced pluripotent stem cell
Iso	Isogenic
KEGG	Kyoto encyclopedia of genes and genomes
LNA-FISH	Locked nucleic acid (LNA) fluorescence in situ hybridization
MEF	Mouse embryonic fibroblast
MN	Motor neuron
MSD	Meso scale discovery immunoassay
Nf-L	Neurofilament light chain
PCA	Principal component analysis
PET	Positron emission tomography
poly(AP)	Poly alanine-proline
poly(GA)	Poly glycine-alanine
poly(GP)	Poly glycine-proline
poly(GR)	Poly glycine-arginine
poly(PR)	Poly proline-arginine
RGC	Radial glial cell
Rm	Membrane resistance
Rs	Series resistance
scRNA-seq	Single-cell RNA sequencing
sEPSC	Spontaneous excitatory post synaptic current
TDP43-ALS	ALS line carrying a mutation in TDP-43
UMAP	Uniform manifold approximation and projection
VLZ	Ventricular-like zone
VNTR-PCR	Variable number tandem repeat PCR

Supplementary Information

The online version contains supplementary material available at https://doi.org/10.1186/s40478-024-01857-1.

Supplementary Material 1. Supplementary Table 2: Top 100 genes per Leiden cluster in scRNA-seq dataset of day 90 cerebral organoids from C9-ALS/FTD patients and healthy controls, plus an overview of cell type annotation process.

Supplementary Material 2. Supplementary Table 3: Differentially expressed genes between C9 and HC within a cell-type cluster from the scRNA-seq dataset of day 90 cerebral organoids.

Supplementary Material 3. Supplementary Table 4: KEGG pathways up- or downregulated in C9 per cell type from the scRNA-seq dataset of day 90 cerebral organoids.

Supplementary Material 4. Supplementary Table 5: Resource table, including antibodies, primers, assays, software, probes and reagents.

Supplementary Material 5. Supplementary Fig. 1: Characterization of C9-ALS/FTD cerebral organoids, Supplementary Fig. 2: C9-HRE causes early accelerated cerebral organoid growth, Supplementary Fig. 3: Quality control single-cell RNA sequencing data and cell type abundance data, Supplementary Fig. 4: Expression of CTIP2 and SOX2 in (pre)symptomatic C9-HRE cerebral organoids and ventricular zone analysis in cerebral organoids using FLSM, Supplementary Fig. 5: Glutamatergic synapse analysis in day 90 cerebral organoids, Supplementary Fig. 6: Characterization of cerebral organoids from presymptomatic C9-HRE carriers, Supplementary Fig. 7: Cerebral organoids from presymptomatic C9-HRE carriers display sense RNA foci from C9-HRE, Supplementary Fig. 8: Cerebral organoids from presymptomatic C9-carriers display phenotypes as observed in C9 organoids, Supplementary Fig. 9: Cell cycle analysis in iPSCs from C9-ALS/FTD patients, Supplementary Table 1: iPSC lines used in this study.

Acknowledgements
We thank Noelia Antón-Bolaños for reading the manuscript. Danielle Vonk, Jasmijn Hundscheid and Svetlana Pasteuning-Vuhman for technical support. Dieter Edbauer for providing reagents.

Author contributions
Conceptualization, A.T.vd.G., R.J.P.; experimental studies, A.T.vd.G., C.E.J., T.L., C.F.H., M.C.L., R.V.d.S., Y.A., M.d.W., D.H.R., M.K., M.M.Z., M.C., E.J.N.G., A.M.I.; clinical data & patient material, H.J.W., L.H.vd.B., J.H.V.; writing–original draft, A.T.vd.G., R.J.P.; writing–review, all; supervision, E.M.H., O.B., A.M.I., D.K.S., R.J.P.; funding acquisition, C.F.H., A.M.I., J.H.V., R.J.P.

Funding
This project was financially supported by Stichting ALS Nederland (TOTALS, ALS-on-a-Chip, MUS-ALS, ATAXALS, GoALS), ALS CURE project, the INTEGRALS consortium (E-Rare-3, the ERANet for Research on Rare Diseases), the EU joint Program Neurodegenerative Diseases (JPND; TRIAGE) (to R.J.P.), a Rudolf Magnus fellowship (to C.F.H.), and the European Research Council (ERC) under the European Union's Horizon 2020 research and innovation programme (Grant Agreement No. 772376 – EScORIAL) (to J.H.V.). A.M.I. is supported by the UK Dementia Research Institute, through UK DRI Ltd, principally funded by the Research Council, and additional funding partners LifeArc and Alzheimer's Research UK.

Availability of data and materials
All data supporting the findings of this study are available within the paper and its Supplementary Information. The scRNA-seq data discussed in this publication have been deposited in NCBI's Gene Expression Omnibus [32] and are accessible through GEO Series accession number GS264012 (https://www.ncbi.nlm.nih.gov/geo/query/acc.cgi?acc=GSE264012).

Declarations

Ethics approval and consent to participate
The medical ethical approval committee (METC) of University Medical Center Utrecht granted approval for iPSC line generation through biobank protocol 16-436. Donors had provided written informed consent. Patients were diagnosed according to the diagnostic criteria for ALS (revised El Escorial). Details of human subjects and iPSC lines can be found in Supplementary Table 1.

Consent for publication
Not applicable.

Competing interests
J.H.V. reports to have sponsored research agreements with Biogen and Astra Zeneca. R.J.P. reports to have sponsored research agreements with Amylyx. The other authors declare no competing interests.

Author details
[1]Department of Translational Neuroscience, UMC Utrecht Brain Center, University Medical Center Utrecht, Utrecht University, Utrecht, The Netherlands.

[2]Department of Neurology and Neurosurgery, UMC Utrecht Brain Center, University Medical Center Utrecht, Utrecht University, Utrecht, The Netherlands. [3]UK Dementia Research Institute at UCL and Dept. of Neurodegenerative Disease, UCL Queen Square Institute of Neurology, London, UK. [4] Department of Genetics, University Medical Center Utrecht, Utrecht University, Utrecht, The Netherlands.

Received: 21 August 2024 Accepted: 24 August 2024
Published online: 18 September 2024

References

1. Abo-Rady M, Kalmbach N, Pal A, Schludi C, Janosch A, Richter T, Freitag P, Bickle M, Kahlert AK, Petri S, Stefanov S, Glass H, Staege S, Just W, Bhatnagar R, Edbauer D, Hermann A, Wegner F, Sterneckert JL (2020) Knocking out C9ORF72 exacerbates axonal trafficking defects associated with hexanucleotide repeat expansion and reduces levels of heat shock proteins. Stem Cell Rep 14:390–405. https://doi.org/10.1016/j.stemcr.2020.01.010
2. Al-Chalabi A, Calvo A, Chiò A, Colville S, Ellis CM, Hardiman O, Heverin M, Howard RS, Huisman MHB, Keren N, Leigh PN, Mazzini L, Mora G, Orrell RW, Rooney J, Scott KM, Scotton WJ, Seelen M, Shaw CE, Sidle KS, Swingler R, Tsuda M, Veldink JH, Visser AE, van den Berg LH, Pearce N (2014) Analysis of amyotrophic lateral sclerosis as a multistep process: a population-based modelling study. Lancet Neurol 13:1108–1113. https://doi.org/10.1016/S1474-4422(14)70219-4
3. Amin ND, Paşca SP (2018) Building models of brain disorders with three-dimensional organoids. Neuron 100:389–405. https://doi.org/10.1016/j.neuron.2018.10.007
4. Arlotta P, Molyneaux BJ, Chen J, Inoue J, Kominami R, MacKlis JD (2005) Neuronal subtype-specific genes that control corticospinal motor neuron development in vivo. Neuron 45:207–221. https://doi.org/10.1016/j.neuron.2004.12.036
5. Arteaga-Bracho EE, Gulinello M, Winchester ML, Pichamoorthy N, Petronglo JR, Zambrano AD, Inocencio J, De Jesus CD, Louie JO, Gokhan S, Mehler MF, Molero AE (2016) Postnatal and adult consequences of loss of huntingtin during development: Implications for Huntington's disease. Neurobiol Dis 96:144–155. https://doi.org/10.1016/j.nbd.2016.09.006
6. Atkinson RAK, Fernandez-Martos CM, Atkin JD, Vickers JC, King AE (2015) C9ORF72 expression and cellular localization over mouse development. Acta Neuropathol Commun 3:59. https://doi.org/10.1186/s40478-015-0238-7
7. Balendra R, Isaacs AM (2018) C9orf72-mediated ALS and FTD: multiple pathways to disease. Nat Rev Neurol 14:544–558. https://doi.org/10.1038/s41582-018-0047-2
8. Barnat M, Capizzi M, Aparicio E, Boluda S, Wennagel D, Kacher R, Kassem R, Lenoir S, Agasse F, Bra BY, Liu JP, Ighil J, Tessier A, Zeitli SO, Duyckaerts C, Dommergues M, Durr A, Humbert S (1979) Huntington's disease alters human neurodevelopment. Science 369:787–793. https://doi.org/10.1126/science.aax3338
9. Bauer CS, Cohen RN, Sironi F, Livesey MR, Gillingwater TH, Highley JR, Fillingham DJ, Coldicott I, Smith EF, Gibson YB, Webster CP, Grierson AJ, Bendotti C, De Vos KJ (2022) An interaction between synapsin and C9orf72 regulates excitatory synapses and is impaired in ALS/FTD. Acta Neuropathol. https://doi.org/10.1007/s00401-022-02470-z
10. Bayer SA, Altman J, Russo RJ, Zhang X (1993) Timetables of neurogenesis in the human brain based on experimentally determined patterns in the rat. Neurotoxicology 14:83–144
11. Bede P, Bokde AL, Byrne S, Marwa Elamin M, Russell McLaughlin ML, Kenna KP, Fagan AJ, Pender N, Bradley DG, Hardiman O (2013) Multiparametric MRI study of ALS stratified for the C9orf72 genotype Results: a congruent pattern of cortical and subcortical involvement was identified in those with the. Neurology 81:361–369. https://doi.org/10.1212/WNL.0b013e31829c5eee
12. Benito-Kwiecinski S, Giandomenico SL, Sutcliffe M, Riis ES, Freire-Pritchett P, Kelava I, Wunderlich S, Martin U, Wray G, Lancaster MA (2020) An early cell shape transition drives evolutionary expansion of the human forebrain. Cell. https://doi.org/10.1101/2020.07.04.188078
13. Bertrand A, Wen J, Rinaldi D, Houot M, Sayah S, Camuzat A, Fournier C, Fontanella S, Routier A, Couratier P, Pasquier F, Habert M-O, Hannequin D, Martinaud O, Caroppo P, Levy R, Dubois B, Brice A, Durrleman S, Colliot O, Le Ber I (2018) Early cognitive, structural, and microstructural changes in presymptomatic C9orf72 carriers younger than 40 years. JAMA Neurol 75:236–245. https://doi.org/10.1001/jamaneurol.2017.4266
14. Bhaduri A, Andrews MG, Mancia Leon W, Jung D, Shin D, Allen DE, Jung D, Schmunk G, Haeussler M, Salma J, Pollen AA, Nowakowski TJ, Kriegstein AR (2020) Cell stress in cortical organoids impairs molecular subtype specification. Nature 578:142–148. https://doi.org/10.1038/s41586-020-1962-0
15. Birtele M, Del Dosso A, Xu T, Nguyen T, Wilkinson B, Hosseini N, Nguyen S, Urenda J, Knight G, Rojas C, Flores I, Atamian A, Moore R, Sharma R, Pirrotte P, Ashton RS, Huang EJ, Rumbaugh G, Coba MP, Quadrato G (2023) Non-synaptic function of the autism spectrum disorder-associated gene SYNGAP1 in cortical neurogenesis. Nat Neurosci. https://doi.org/10.1038/s41593-023-01477-3
16. Le Blanc G, Jetté Pomerleau V, McCarthy J, Borroni B, van Swieten J, Galimberti D, Sanchez-Valle R, LaForce R, Moreno F, Synofzik M, Graff C, Masellis M, Tartaglia MC, Rowe JB, Vandenberghe R, Finger E, Tagliavini F, de Mendonça A, Santana I, Butler C, Gerhard A, Danek A, Levin J, Otto M, Frisoni G, Sorbi S, Rohrer JD, Ducharme S (2020) Faster cortical thinning and surface area loss in presymptomatic and symptomatic C9orf72 repeat expansion adult carriers. Ann Neurol 88:113–122. https://doi.org/10.1002/ana.25748
17. Broce IJ, Sirkis DW, Nillo RM, Bonham LW, Lee SE, Miller BL, Castruita PA, Sturm VE, Sugrue LS, Desikan RS, Yokoyama JS (2024) C9orf72 gene networks in the human brain correlate with cortical thickness in C9-FTD and implicate vulnerable cell types. Front Neurosci 18:1–15. https://doi.org/10.3389/fnins.2024.1258996
18. Van Der Burgh HK, Westeneng HJ, Walhout R, Van Veenhuijzen K, Tan HHG, Meier JM, Bakker LA, Hendrikse J, Van Es MA, Veldink JH, Van Den Heuvel MP, Van Den Berg LH (2020) Multimodal longitudinal study of structural brain involvement in amyotrophic lateral sclerosis. Neurology 94:E2592–E2604. https://doi.org/10.1212/WNL.0000000000009498
19. Burk K, Pasterkamp RJ (2019) Disrupted neuronal trafficking in amyotrophic lateral sclerosis. Acta Neuropathol 137:859–877. https://doi.org/10.1007/s00401-019-01964-7
20. Burley S, Beccano-Kelly DA, Talbot K, Llana OC, Wade-Martins R (2022) Hyperexcitability in young iPSC-derived C9ORF72 mutant motor neurons is associated with increased intracellular calcium release. Sci Rep 12:1–8. https://doi.org/10.1038/s41598-022-09751-3
21. Butti Z, Pan YE, Giacomotto J, Patten SA (2021) Reduced C9orf72 function leads to defective synaptic vesicle release and neuromuscular dysfunction in zebrafish. Commun Biol 4:792. https://doi.org/10.1038/s42003-021-02302-y
22. Büttner M, Ostner J, Müller CL, Theis FJ, Schubert B (2021) scCODA is a Bayesian model for compositional single-cell data analysis. Nat Commun 12:1–10. https://doi.org/10.1038/s41467-021-27150-6
23. Camp JG, Badsha F, Florio M, Kanton S, Gerber T, Wilsch-Bräuninger M, Lewitus E, Sykes A, Hevers W, Lancaster MA, Knoblich JA, Lachmann R, Pääbo S, Huttner WB, Treutlein B (2015) Human cerebral organoids recapitulate gene expression programs of fetal neocortex development. Proc Natl Acad Sci USA 112:15672–15677. https://doi.org/10.1073/pnas.1520760112
24. Catanese A, Rajkumar S, Sommer D, Freisem D, Wirth A, Aly A, Massa-López D, Olivieri A, Torelli F, Ioannidis V, Lipecka J, Guerrera IC, Zytnicki D, Ludolph A, Kabashi E, Mulaw MA, Roselli F, Böckers TM (2021) Synaptic disruption and CREB-regulated transcription are restored by K + channel blockers in ALS. EMBO Mol Med 13:1–16. https://doi.org/10.15252/emmm.202013131
25. Cheroni C, Trattaro S, Caporale N, López-Tobón A, Tenderini E, Sebastiani S, Troglio F, Gabriele M, Bressan RB, Pollard SM, Gibson WT, Testa G (2022) Benchmarking brain organoid recapitulation of fetal corticogenesis. Transl Psychiatry. https://doi.org/10.1038/s41398-022-02279-0
26. Choi SY, Lopez-Gonzalez R, Krishnan G, Phillips HL, Li AN, Seeley WW, Yao WD, Almeida S, Gao FB (2019) C9ORF72-ALS/FTD-associated poly(GR) binds Atp5a1 and compromises mitochondrial function in vivo. Nat Neurosci 22:851–862. https://doi.org/10.1038/s41593-019-0397-0

27. Clayton EL, Huggon L, Cousin MA, Mizielinska S (2024) Synaptopathy: presynaptic convergence in frontotemporal dementia and amyotrophic lateral sclerosis. Brain 139:16–17. https://doi.org/10.1093/brain/awae074
28. Dafinca R, Barbagallo P, Farrimond L, Candalija A, Scaber J, Ababneh NA, Sathyaprakash C, Vowles J, Cowley SA, Talbot K (2020) Impairment of mitochondrial calcium buffering links mutations in C9ORF72 and TARDBP in iPS-derived motor neurons from patients with ALS/FTD. Stem Cell Rep 14:892–908. https://doi.org/10.1016/j.stemcr.2020.03.023
29. DeJesus-Hernandez M, Mackenzie IRA, Boeve BF, Boxer AL, Baker MC, Rutherford NJ, Nicholson AM, Finch NA, Flynn H, Adamson J, Kouri N, Wojtas AM, Sengdy P, Hsiung G-YR, Karydas A, Seeley WW, Josephs KA, Coppola G, Geschwind DH, Wszolek ZK, Feldman H, Knopman DS, Petersen RC, Miller BL, Dickson DW, Boylan KB, Graff-Radford NR, Rademakers R (2011) Expanded GGGGCC hexanucleotide repeat in noncoding region of C9ORF72 causes chromosome 9p-Linked FTD and ALS. Neuron 72:245–256. https://doi.org/10.1016/j.neuron.2011.09.011
30. Devlin AC, Burr K, Borooah S, Foster JD, Cleary EM, Geti I, Vallier L, Shaw CE, Chandran S, Miles GB (2015) Human iPSC-derived motoneurons harbouring TARDBP or C9ORF72 ALS mutations are dysfunctional despite maintaining viability. Nat Commun 6:1–12. https://doi.org/10.1038/ncomms6999
31. Dorst J, Weydt P, Brenner D, Witzel S, Kandler K, Huss A, Herrmann C, Wiesenfarth M, Knehr A, Günther K, Müller K, Weishaupt JH, Prudlo J, Forsberg K, Andersen PM, Rosenbohm A, Schuster J, Roselli F, Dupuis L, Mayer B, Tumani H, Kassubek J, Ludolph AC (2023) Metabolic alterations precede neurofilament changes in presymptomatic ALS gene carriers. EBioMedicine 90:104521. https://doi.org/10.1016/j.ebiom.2023.104521
32. Edgar R, Domrachev M, Lash AE (2002) Gene expression omnibus: NCBI gene expression and hybridization array data repository. Nucleic Acids Res 30:207–210. https://doi.org/10.1093/nar/30.1.207
33. Van Es MA, Hardiman O, Chiò A, Al-Chalabi A, Pasterkamp RJ, Veldink JH, van den Berg LH (2017) Amyotrophic lateral sclerosis. Lancet 390:2084–2098. https://doi.org/10.1016/S0140-6736(17)31287-4
34. Ferguson R, Serafeimidou-Pouliou E, Subramanian V (2016) Dynamic expression of the mouse orthologue of the human amyotropic lateral sclerosis associated gene C9orf72 during central nervous system development and neuronal differentiation. J Anat 229:871–891. https://doi.org/10.1111/joa.12526
35. Floeter MK, Bageac D, Danielian LE, Braun LE, Traynor BJ, Kwan JY (2016) Longitudinal imaging in C9orf72 mutation carriers: relationship to phenotype. Neuroimage Clin 12:1035–1043. https://doi.org/10.1016/j.nicl.2016.10.014
36. Freibaum BD, Lu Y, Lopez-Gonzalez R, Kim NC, Almeida S, Lee KH, Badders N, Valentine M, Miller BL, Wong PC, Petrucelli L, Kim HJ, Gao FB, Taylor JP (2015) GGGGCC repeat expansion in C9orf72 compromises nucleocytoplasmic transport. Nature 525:129–133. https://doi.org/10.1038/nature14974
37. Frick P, Sellier C, Mackenzie IRA, Cheng CY, Tahraoui-Bories J, Martinat C, Pasterkamp RJ, Prudlo J, Edbauer D, Oulad-Abdelghani M, Feederle R, Charlet-Berguerand N, Neumann M (2018) Novel antibodies reveal presynaptic localization of C9orf72 protein and reduced protein levels in C9orf72 mutation carriers. Acta Neuropathol Commun 6:72. https://doi.org/10.1186/s40478-018-0579-0
38. Fumagalli L, Young FL, Boeynaems S, De Decker M, Mehta AR, Swijsen A, Fazal R, Guo W, Moisse M, Beckers J, Dedeene L, Selvaraj BT, Vandoorne T, Madan V, van Blitterswijk M, Raitcheva D, McCampbell A, Poesen K, Gitler AD, Koch P, Vanden BP, Thal DR, Verfaillie C, Chandran S, Van Den Bosch L, Bullock SL, Van Damme P (2021) C9orf72 -derived arginine-containing dipeptide repeats associate with axonal transport machinery and impede microtubule-based motility. Sci Adv. https://doi.org/10.1126/sciadv.abg3013
39. Gao C, Shi Q, Pan X, Chen J, Zhang Y, Lang J, Wen S, Liu X, Cheng T-L, Lei K (2024) Neuromuscular organoids model spinal neuromuscular pathologies in C9orf72 amyotrophic lateral sclerosis. Cell Rep 43:113892. https://doi.org/10.1016/j.celrep.2024.113892
40. Garrido D, Beretta S, Grabrucker S, Bauer HF, Bayer D, Sala C, Verpelli C, Roselli F, Bockmann J, Proepper C, Catanese A, Boeckers TM (2022) Shank2/3 double knockout-based screening of cortical subregions links the retrosplenial area to the loss of social memory in autism spectrum disorders. Mol Psychiatry 27:4994–5006. https://doi.org/10.1038/s41380-022-01756-8
41. Geevasinga N, Menon P, Nicholson GA, Ng K, Howells J, Kril JJ, Yiannikas C, Kiernan MC, Vucic S (2015) Cortical function in asymptomatic carriers and patients with C9Orf72 amyotrophic lateral sclerosis. JAMA Neurol 72:1268–1274. https://doi.org/10.1001/jamaneurol.2015.1872
42. Gelon PA, Dutchak PA, Sephton CF (2022) Synaptic dysfunction in ALS and FTD: anatomical and molecular changes provide insights into mechanisms of disease. Front Mol Neurosci. https://doi.org/10.3389/fnmol.2022.1000183
43. Giacomelli E, Vahsen BF, Calder EL, Xu Y, Scaber J, Gray E, Dafinca R, Talbot K, Studer L (2022) Human stem cell models of neurodegeneration: From basic science of amyotrophic lateral sclerosis to clinical translation. Cell Stem Cell 29:11–35. https://doi.org/10.1016/j.stem.2021.12.008
44. Giandomenico SL, Mierau SB, Gibbons GM, Wenger LMD, Masullo L, Sit T, Sutcliffe M, Boulanger J, Tripodi M, Derivery E, Paulsen O, Lakatos A, Lancaster MA (2019) Cerebral organoids at the air–liquid interface generate diverse nerve tracts with functional output. Nat Neurosci 22:669–679. https://doi.org/10.1038/s41593-019-0350-2
45. Gittings LM, Alsop EB, Antone J, Singer M, Whitsett TG, Sattler R, Jensen KVK (2023) Cryptic exon detection and transcriptomic changes revealed in single—nuclei RNA sequencing of C9ORF72 patients spanning the ALS—FTD spectrum. Acta Neuropathol. https://doi.org/10.1007/s00401-023-02599-5
46. Götz M, Huttner WB (2005) The cell biology of neurogenesis. Nat Rev Mol Cell Biol 6:777–788. https://doi.org/10.1038/nrm1739
47. Harschnitz O, van den Berg LH, Johansen LE, Jansen MD, Kling S, Vieira de Sá R, Vlam L, van Rheenen W, Karst H, Wierenga CJ, Pasterkamp RJ, van der Pol WL (2016) Autoantibody pathogenicity in a multifocal motor neuropathy induced pluripotent stem cell–derived model. Ann Neurol 80:71–88. https://doi.org/10.1002/ana.24680
48. Hendricks E, Quihuis AM, Hung S, Chang J, Dorjsuren N, Der B, Staats KA, Shi Y, Sta Maria NS, Jacobs RE, Ichida JK (2023) The C9ORF72 repeat expansion alters neurodevelopment. Cell Rep 42:112983. https://doi.org/10.1016/j.celrep.2023.112983
49. Ho WY, Tai YK, Chang JC, Liang J, Tyan SH, Chen S, Guan JL, Zhou H, Shen HM, Koo E, Ling SC (2019) The ALS-FTD-linked gene product, C9orf72, regulates neuronal morphogenesis via autophagy. Autophagy 15:827–842. https://doi.org/10.1080/15548627.2019.1569441
50. Huber N, Hoffmann D, Giniatullina R, Rostalski H, Leskelä S, Takalo M, Natunen T, Solje E, Remes AM, Giniatullin R, Hiltunen M, Haapasalo A (2022) C9orf72 hexanucleotide repeat expansion leads to altered neuronal and dendritic spine morphology and synaptic dysfunction. Neurobiol Dis. https://doi.org/10.1016/j.nbd.2021.105584
51. Hung ST, Linares GR, Chang WH, Eoh Y, Krishnan G, Mendonca S, Hong S, Shi Y, Santana M, Kueth C, Macklin-Isquierdo S, Perry S, Duhaime S, Maios C, Chang J, Perez J, Couto A, Lai J, Li Y, Alworth SV, Hendricks E, Wang Y, Zlokovic BV, Dickman DK, Parker JA, Zarnescu DC, Gao FB, Ichida JK (2023) PIKFYVE inhibition mitigates disease in models of diverse forms of ALS. Cell 186:786-802.e28. https://doi.org/10.1016/j.cell.2023.01.005
52. Irwin KE, Jasin P, Braunstein KE, Sinha IR, Garret MA, Bowden KD, Chang K, Troncoso JC, Moghekar A, Oh ES, Raitcheva D, Bartlett D, Miller T, Berry JD, Traynor BJ, Ling JP, Wong PC (2024) A fluid biomarker reveals loss of TDP-43 splicing repression in presymptomatic ALS–FTD. Nature Med 30:382–393. https://doi.org/10.1038/s41591-023-02788-5
53. Kan AA, van Erp S, Derijck AAHA, de Wit M, Hessel EVS, O'Duibhir E, de Jager W, van Rijen PC, Gosselaar PH, de Graan PNE, Pasterkamp RJ (2012) Genome-wide microRNA profiling of human temporal lobe epilepsy identifies modulators of the immune response. Cell Mol Life Sci 69:3127–3145. https://doi.org/10.1007/S00018-012-0992-7
54. Kanehisa M (2000) KEGG: kyoto encyclopedia of genes and genomes. Nucleic Acids Res 28:27–30. https://doi.org/10.1093/nar/28.1.27
55. Kanehisa M, Furumichi M, Sato Y, Kawashima M, Ishiguro-Watanabe M (2023) KEGG for taxonomy-based analysis of pathways and genomes. Nucleic Acids Res 51:D587–D592. https://doi.org/10.1093/nar/gkac963
56. Kanton S, Boyle MJ, He Z, Santel M, Weigert A, Sanchís-Calleja F, Guijarro P, Sidow L, Fleck JS, Han D, Qian Z, Heide M, Huttner WB, Khaitovich P, Pääbo S, Treutlein B, Camp JG (2019) Organoid single-cell genomic

atlas uncovers human-specific features of brain development. Nature 574:418–422. https://doi.org/10.1038/s41586-019-1654-9
57. Katrukha E (2022) ekatrukha/ComDet: ComDet 0.5.5
58. Kelava I, Lancaster MA (2016) Stem cell models of human brain development. Cell Stem Cell 18:736–748. https://doi.org/10.1016/j.stem.2016.05.022
59. Lall D, Lorenzini I, Mota TA, Bell S, Mahan TE, Ulrich JD, Davtyan H, Rexach JE, Muhammad AKMG, Shelest O, Landeros J, Vazquez M, Kim J, Ghaffari LT, O'Rourke JG, Geschwind DH, Blurton-Jones M, Holtzman DM, Sattler R, Baloh RH (2021) C9orf72 deficiency promotes microglial-mediated synaptic loss in aging and amyloid accumulation. Neuron. https://doi.org/10.1016/j.neuron.2021.05.020
60. Lancaster MA, Knoblich JA (2014) Generation of cerebral organoids from human pluripotent stem cells. Nat Protoc 9:2329–2340. https://doi.org/10.1038/nprot.2014.158
61. Lancaster MA, Renner M, Martin C-A, Wenzel D, Bicknell LS, Hurles ME, Homfray T, Penninger JM, Jackson AP, Knoblich JA (2013) Cerebral organoids model human brain development and microcephaly. Nature 501:373–379. https://doi.org/10.1038/nature12517
62. Landry CR, Yip MC, Zhou Y, Niu W, Wang Y, Yang B, Wen Z, Forest CR (2023) Electrophysiological and morphological characterization of single neurons in intact human brain organoids. J Neurosci Methods 394:109898. https://doi.org/10.1016/j.jneumeth.2023.109898
63. Lee H, Mackenzie IRA, Beg MF, Popuri K, Rademakers R, Wittenberg D, Hsiung GR (2022) White-matter abnormalities in presymptomatic GRN and C9orf72 mutation carriers. Brain Commun 5:1–12. https://doi.org/10.1093/braincomms/fcac333
64. Lee SE, Sias AC, Mandelli ML, Brown JA, Brown AB, Khazenzon AM, Vidovszky AA, Zanto TP, Karydas AM, Pribadi M, Dokuru D, Coppola G, Geschwind DH, Rademakers R, Gorno-Tempini ML, Rosen HJ, Miller BL, Seeley WW (2017) Network degeneration and dysfunction in presymptomatic C9ORF72 expansion carriers. Neuroimage Clin 14:286–297. https://doi.org/10.1016/j.nicl.2016.12.006
65. van de Leemput J, Boles NC, Kiehl TR, Corneo B, Lederman P, Menon V, Lee C, Martinez RA, Levi BP, Thompson CL, Yao S, Kaykas A, Temple S, Fasano CA (2014) CORTECON: a temporal transcriptome analysis of in vitro human cerebral cortex development from human embryonic stem cells. Neuron 83:51–68. https://doi.org/10.1016/j.neuron.2014.05.013
66. Li J, Jaiswal MK, Chien J, Kozlenkov A, Jung J, Zhou P, Gardashli M, Pregent LJ, Engelberg-Cook E, Dickson DW, Belzil VV, Mukamel EA, Dracheva S (2023) Divergent single cell transcriptome and epigenome alterations in ALS and FTD patients with C9orf72 mutation. Nat Commun 14:5714. https://doi.org/10.1038/s41467-023-41033-y
67. Longinetti E, Fang F (2019) Epidemiology of amyotrophic lateral sclerosis: an update of recent literature. Curr Opin Neurol 32:771–776. https://doi.org/10.1097/WCO.0000000000000730
68. Lopez-Gonzalez R (2023) Cell cycle dysregulation in iPSC-derived neurons from C9ORF72 carriers. Alzheimer's Dementia 19:83264. https://doi.org/10.1002/alz.083264
69. Lule DE, Müller HP, Finsel J, Weydt P, Knehr A, Winroth I, Andersen PM, Weishaupt JH, Uttner I, Kassubek J, Ludolph AC (2020) Deficits in verbal fluency in presymptomatic C9orf72 mutation gene carriers—a developmental disorder. J Neurol Neurosurg Psychiatry 91:1195–1200. https://doi.org/10.1136/jnnp-2020-323671
70. MacDonald JL, Fame RM, Azim E, Shnider SJ, Molyneaux BJ, Arlotta P, Macklis JD (2013) Specification of cortical projection neurons. In: Patterning and cell type specification in the developing CNS and PNS. Elsevier, pp 475–502
71. Mackenzie IRA, Frick P, Grässer FA, Gendron TF, Petrucelli L, Cashman NR, Edbauer D, Kremmer E, Prudlo J, Troost D, Neumann M (2015) Quantitative analysis and clinico-pathological correlations of different dipeptide repeat protein pathologies in C9ORF72 mutation carriers. Acta Neuropathol 130:845–861. https://doi.org/10.1007/s00401-015-1476-2
72. Mackenzie IRA, Frick P, Neumann M (2014) The neuropathology associated with repeat expansions in the C9ORF72 gene. Acta Neuropathol 127:347–357. https://doi.org/10.1007/s00401-013-1232-4
73. Malpetti M, Holland N, Jones PS, Ye R, Cope TE, Fryer TD, Hong YT, Savulich G, Rittman T, Passamonti L, Mak E, Aigbirhio FI, O'Brien JT, Rowe JB (2021) Synaptic density in carriers of C9orf72 mutations: a [11C]UCB-J PET study. Ann Clin Transl Neurol 8:1515–1523. https://doi.org/10.1002/acn3.51407
74. Marin Navarro A, Pronk RJ, van der Geest AT, Oliynyk G, Nordgren A, Arsenian-Henriksson M, Falk A, Wilhelm M, Navarro AM, Pronk RJ, Van Der GAT, Oliynyk G, Nordgren A, Arsenian-Henriksson M, Falk A, Wilhelm M (2020) p53 controls genomic stability and temporal differentiation of human neural stem cells and affects neural organization in human brain organoids. Cell Death Dis 11:52. https://doi.org/10.1038/s41419-019-2208-7
75. McInnes L, Healy J, Melville J (2020) UMAP: uniform manifold approximation and projection for dimension reduction
76. Menon P, Higashihara M, van den Bos M, Geevasinga N, Kiernan MC, Vucic S (2020) Cortical hyperexcitability evolves with disease progression in ALS. Ann Clin Transl Neurol 7:733–741. https://doi.org/10.1002/acn3.51039
77. Menon P, Kiernan MC, Vucic S (2015) Cortical hyperexcitability precedes lower motor neuron dysfunction in ALS. Clin Neurophysiol 126:803–809. https://doi.org/10.1016/j.clinph.2014.04.023
78. Molyneaux BJ, Arlotta P, Hirata T, Hibi M, Macklis JD (2005) Fezl is required for the birth and specification of corticospinal motor neurons. Neuron 47:817–831. https://doi.org/10.1016/j.neuron.2005.08.030
79. Molyneaux BJ, Arlotta P, Menezes JRL, Macklis JD (2007) Neuronal subtype specification in the cerebral cortex. Nat Rev Neurosci 8:427–437. https://doi.org/10.1038/nrn2151
80. Mori K, Weng SM, Arzberger T, May S, Rentzsch K, Kremmer E, Schmid B, Kretzschmar HA, Cruts M, Van Broeckhoven C, Haass C (1979) Edbauer D (2013) The C9orf72 GGGGCC repeat is translated into aggregating dipeptide-repeat proteins in FTLD/ALS. Science 339:1335–1338. https://doi.org/10.1126/science.1232927
81. Murphy NA, Arthur KC, Tienari PJ, Houlden H, Chiò A, Traynor BJ (2017) Age-related penetrance of the C9orf72 repeat expansion. Sci Rep 7:1–7. https://doi.org/10.1038/s41598-017-02364-1
82. Nigri A, Umberto M, Stanziano M, Ferraro S, Fedeli D, Medina Carrion JP, Palermo S, Lequio L, Denegri F, Agosta F, Filippi M, Valentini MC, Canosa A, Calvo A, Chiò A, Bruzzone MG, Moglia C (2023) C9orf72 ALS mutation carriers show extensive cortical and subcortical damage compared to matched wild-type ALS patients. Neuroimage Clin 38:103400. https://doi.org/10.1016/j.nicl.2023.103400
83. Ormel PR, Vieira de Sá R, van Bodegraven EJ, Karst H, Harschnitz O, Sneeboer MAM, Johansen LE, van Dijk RE, Scheefhals N, Berdenis van Berlekom A, Ribes Martínez E, Kling S, MacGillavry HD, van den Berg LH, Kahn RS, Hol EM, de Witte LD, Pasterkamp RJ (2018) Microglia innately develop within cerebral organoids. Nat Commun 9:4167. https://doi.org/10.1038/s41467-018-06684-2
84. Pașca AM, Park JY, Shin HW, Qi Q, Revah O, Krasnoff R, O'Hara R, Willsey AJ, Palmer TD, Pașca SP (2019) Human 3D cellular model of hypoxic brain injury of prematurity. Nat Med. https://doi.org/10.1038/s41591-019-0436-0
85. Perkins EM, Burr K, Banerjee P, Mehta AR, Dando O, Selvaraj BT, Suminaite D, Nanda J, Henstridge CM, Gillingwater TH, Hardingham GE, Wyllie DJA, Chandran S, Livesey MR (2021) Altered network properties in C9ORF72 repeat expansion cortical neurons are due to synaptic dysfunction. Mol Neurodegener 16:1–16. https://doi.org/10.1186/s13024-021-00433-8
86. Pineda SS, Lee H, Ulloa-Navas MJ, Linville RM, Garcia FJ, Galani K, Engelberg-Cook E, Castanedes MC, Fitzwalter BE, Pregent LJ, Gardashli ME, DeTure M, Vera-Garcia DV, Hucke ATS, Oskarsson BE, Murray ME, Dickson DW, Heiman M, Belzil VV, Kellis M (2024) Single-cell dissection of the human motor and prefrontal cortices in ALS and FTLD. Cell. https://doi.org/10.1016/j.cell.2024.02.031
87. Porterfield V, Khan SS, Foff EP, Koseoglu MM, Blanco IK, Jayaraman S, Lien E, McConnell MJ, Bloom GS, Lazo JS, Sharlow ER (2020) A three-dimensional dementia model reveals spontaneous cell cycle re-entry and a senescence-associated secretory phenotype. Neurobiol Aging 90:125–134. https://doi.org/10.1016/j.neurobiolaging.2020.02.011
88. Proudfoot M, Gutowski NJ, Edbauer D, Hilton DA, Stephens M, Rankin J, Mackenzie IRA (2014) Early dipeptide repeat pathology in a frontotemporal dementia kindred with C9ORF72 mutation and intellectual disability. Acta Neuropathol 127:451–458. https://doi.org/10.1007/s00401-014-1245-7

89. Quadrato G, Nguyen T, Macosko EZ, Sherwood JL, Min Yang S, Berger DR, Maria N, Scholvin J, Goldman M, Kinney JP, Boyden ES, Lichtman JW, Williams ZM, McCarroll SA, Arlotta P (2017) Cell diversity and network dynamics in photosensitive human brain organoids. Nature 545:48–53. https://doi.org/10.1038/nature22047
90. Renier N, Adams EL, Kirst C, Wu Z, Azevedo R, Kohl J, Autry AE, Kadiri L, Umadevi Venkataraju K, Zhou Y, Wang VX, Tang CY, Olsen O, Dulac C, Osten P, Tessier-Lavigne M (2016) Mapping of brain activity by automated volume analysis of immediate early genes. Cell 165:1789–1802. https://doi.org/10.1016/j.cell.2016.05.007
91. Renier N, Wu Z, Simon DJ, Yang J, Ariel P, Tessier-Lavigne M (2014) iDISCO: a simple, rapid method to immunolabel large tissue samples for volume imaging. Cell 159:896–910. https://doi.org/10.1016/j.cell.2014.10.010
92. Renton AE, Majounie E, Waite AJ, Simón-Sánchez J, Rollinson S, Gibbs JR, Schymick JC, Laaksovirta H, van Swieten JC, Myllykangas L, Kalimo H, Paetau A, Abramzon Y, Remes AM, Kaganovich A, Scholz SW, Duckworth J, Ding J, Harmer DW, Hernandez DG, Johnson JO, Mok K, Ryten M, Trabzuni D, Guerreiro RJ, Orrell RW, Neal J, Murray A, Pearson J, Jansen IE, Sondervan D, Seelaar H, Blake DJ, Young K, Halliwell N, Callister JB, Toulson G, Richardson A, Gerhard A, Snowden J, Mann DMA, Neary D, Nalls MA, Peuralinna T, Jansson L, Isoviita VM, Kaivorinne AL, Hölttä-Vuori M, Ikonen E, Sulkava R, Benatar M, Wuu J, Chiò A, Restagno G, Borghero G, Sabatelli M, Heckerman D, Rogaeva E, Zinman L, Rothstein JD, Sendtner M, Drepper C, Eichler EE, Alkan C, Abdullaev Z, Pack SD, Dutra A, Pak E, Hardy J, Singleton AB, Williams NM, Heutink P, Pickering-Brown S, Morris HR, Tienari PJ, Traynor BJ (2011) A hexanucleotide repeat expansion in C9ORF72 is the cause of chromosome 9p21-linked ALS-FTD. Neuron 72:257–268. https://doi.org/10.1016/j.neuron.2011.09.010
93. Rohrer JD, Nicholas JM, Cash DM, van Swieten J, Dopper E, Jiskoot L, van Minkelen R, Rombouts SA, Cardoso MJ, Clegg S, Espak M, Mead S, Thomas DL, De Vita E, Masellis M, Black SE, Freedman M, Keren R, MacIntosh BJ, Rogaeva E, Tang-Wai D, Tartaglia MC, Laforce R, Tagliavini F, Tiraboschi P, Redaelli V, Prioni S, Grisoli M, Borroni B, Padovani A, Galimberti D, Scarpini E, Arighi A, Fumagalli G, Rowe JB, Coyle-Gilchrist I, Graff C, Fallström M, Jelic V, Ståhlbom AK, Andersson C, Thonberg H, Lilius L, Frisoni GB, Pievani M, Bocchetta M, Benussi L, Ghidoni R, Finger E, Sorbi S, Nacmias B, Lombardi G, Polito C, Warren JD, Ourselin S, Fox NC, Rossor MN (2015) Presymptomatic cognitive and neuroanatomical changes in genetic frontotemporal dementia in the Genetic Frontotemporal dementia Initiative (GENFI) study: a cross-sectional analysis. Lancet Neurol 14:253–262. https://doi.org/10.1016/S1474-4422(14)70324-2
94. Ryan M, Doherty MA, Al Khleifat A, Costello E, Hengeveld JC, Heverin M, Al-Chalabi A, Mclaughlin RL, Hardiman O (2024) C9orf72 repeat expansion discordance in 6 multigenerational kindreds. Neurol Genet 10:1–9. https://doi.org/10.1212/NXG.0000000000200112
95. Rybak-Wolf A, Wyler E, Pentimalli TM, Legnini I, Oliveras Martinez A, Glažar P, Loewa A, Kim SJ, Kaufer BB, Woehler A, Landthaler M, Rajewsky N (2023) Modelling viral encephalitis caused by herpes simplex virus 1 infection in cerebral organoids. Nat Microbiol 8:1252–1266. https://doi.org/10.1038/s41564-023-01405-y
96. Sances S, Bruijn LI, Chandran S, Eggan K, Ho R, Klim JR, Livesey MR, Lowry E, Macklis JD, Rushton D, Sadegh C, Sareen D, Wichterle H, Zhang S-C, Svendsen CN (2016) Modeling ALS with motor neurons derived from human induced pluripotent stem cells. Nat Neurosci 19:542–553. https://doi.org/10.1038/nn.4273
97. Saracino D, Le Ber I (2022) How can we define the presymptomatic C9orf72 disease in 2022? An overview on the current definitions of preclinical and prodromal phases. Rev Neurol (Paris) 178:426–436. https://doi.org/10.1016/j.neurol.2022.03.007
98. Sareen D, O'Rourke JG, Meera P, Muhammad AKMG, Grant S, Simpkinson M, Bell S, Carmona S, Ornelas L, Sahabian A, Gendron TF, Petrucelli L, Baughn M, Ravits J, Harms MB, Rigo F, Frank Bennett C, Otis TS, Svendsen CN, Baloh RH (2013) Targeting RNA foci in iPSC-derived motor neurons from ALS patients with a C9ORF72 repeat expansion. Sci Transl Med. https://doi.org/10.1126/scitranslmed.3007529
99. Schmeisser K, Parker JA (2018) Nicotinamide-N-methyltransferase controls behavior, neurodegeneration and lifespan by regulating neuronal autophagy
100. Hafiei G, Bazinet V, Dadar M, Manera AL, Collins DL, Dagher A, Borroni B, Sanchez-Valle R, Moreno F, Laforce R, Graff C, Synofzik M, Galimberti D, Rowe JB, Masellis M, Tartaglia MC, Finger E, Vandenberghe R, de Mendonça A, Tagliavini F, Santana I, Butler C, Gerhard A, Danek A, Levin J, Otto M, Sorbi S, Jiskoot LC, Seelaar H, van Swieten JC, Rohrer JD, Misic B, Ducharme S, Rosen H, Dickerson BC, Domoto-Reilly K, Knopman D, Boeve BF, Boxer AL, Kornak J, Miller BL, Seeley WW, Gorno-Tempini ML, McGinnis S, Mandelli ML, Esteve AS, Nelson A, Bouzigues A, Heller C, Greaves CV, Cash D, Thomas DL, Todd E, Benotmane H, Zetterberg H, Swift IJ, Nicholas J, Samra K, Russell LL, Bocchetta M, Shafei R, Convery RS, Timberlake C, Cope T, Rittman T, Benussi A, Premi E, Gasparotti R, Archetti S, Gazzina S, Cantoni V, Arighi A, Fenoglio C, Scarpini E, Fumagalli G, Borracci V, Rossi G, Giaccone G, Di Fede G, Caroppo P, Tiraboschi P, Prioni S, Redaelli V, Tang-Wai D, Rogaeva E, Castelo-Branco M, Freedman M, Keren R, Black S, Mitchell S, Shoesmith C, Bartha R, Rademakers R, van DerEnde E, Poos J, Papma JM, Giannini L, van Minkelen R, Pijnenburg Y, Nacmias B, Ferrari C, Polito C, Lombardi G, Bessi V, Veldsman M, Andersson C, Thonberg H, Öijerstedt L, Jelic V, Thompson P, Langheinrich T, Lladó A, Antonell A, Olives J, Balasa M, Bargalló N, Borrego-Ecija S, Verdelho A, Maruta C, Ferreira CB, Miltenberger G, Simões do Couto F, Gabilondo A, Gorostidi A, Villanua J, Cañada M, Tainta M, Zulaica M, Barandiaran M, Alves P, Bender B, Wilke C, Graf L, Vogels A, Vandenbulcke M, Van Damme P, Bruffaerts R, Rosa-Neto P, Gauthier S, Camuzat A, Brice A, Bertrand A, Funkiewiez A, Rinaldi D, Saracino D, Colliot O, Sayah S, Prix C, Wlasich E, Wagemann O, Loosli S, Schönecker S, Hoegen T, Lombardi J, Anderl-Straub S, Rollin A, Kuchcinski G, Bertoux M, Lebouvier T, Deramecourt V, Santiago B, Duro D, Leitão MJ, Almeida MR, Tábuas-Pereira M, Afonso S, Engel A, Polyakova M (2023) Network structure and transcriptomic vulnerability shape atrophy in frontotemporal dementia. Brain 146:321–336. https://doi.org/10.1093/brain/awac069
101. Shi Y, Lin S, Staats KA, Li Y, Chang W-H, Hung S-T, Hendricks E, Linares GR, Wang Y, Son EY, Wen X, Kisler K, Wilkinson B, Menendez L, Sugawara T, Woolwine P, Huang M, Cowan MJ, Ge B, Koutsodendris N, Sandor KP, Komberg J, Vangoor VR, Senthilkumar K, Hennes V, Seah C, Nelson AR, Cheng T-Y, Lee S-JJ, August PR, Chen JA, Wisniewski N, Hanson-Smith V, Belgard TG, Zhang A, Coba MP, Grunseich C, Ward ME, van den Berg LH, Pasterkamp RJ, Trotti D, Zlokovic BV, Ichida JK (2018) Haploinsufficiency leads to neurodegeneration in C9ORF72 ALS/FTD human induced motor neurons. Nat Med 24:313–325. https://doi.org/10.1038/nm.4490
102. Shoemaker LD, Arlotta P (2010) Untangling the cortex: Advances in understanding specification and differentiation of corticospinal motor neurons. BioEssays 32:197–206. https://doi.org/10.1002/bies.200900114
103. Simone R, Balendra R, Moens TG, Preza E, Wilson KM, Heslegrave A, Woodling NS, Niccoli T, Gilbert-Jaramillo J, Abdelkarim S, Clayton EL, Clarke M, Konrad M, Nicoll AJ, Mitchell JS, Calvo A, Chiò A, Houlden H, Polke JM, Ismail MA, Stephens CE, Vo T, Farahat AA, Wilson WD, Boykin DW, Zetterberg H, Partridge L, Wray S, Parkinson G, Neidle S, Patani R, Fratta P, Isaacs AM (2018) G-quadruplex-binding small molecules ameliorate C9orf72 FTD/ALS pathology in vitro and in vivo. EMBO Mol Med 10:22–31. https://doi.org/10.15252/emmm.201707850
104. Smeyers J, Banchi E-G, Latouche M (2021) C9ORF72: what it is, what it does, and why it matters. Front Cell Neurosci 15:1–16. https://doi.org/10.3389/fncel.2021.661447
105. Sommer D, Rajkumar S, Seidel M, Aly A, Ludolph A, Ho R, Boeckers TM, Catanese A (2022) Aging-dependent altered transcriptional programs underlie activity impairments in human C9orf72-mutant motor neurons. Front Mol Neurosci 15:1–17. https://doi.org/10.3389/fnmol.2022.894230
106. Starr A, Sattler R (2018) Synaptic dysfunction and altered excitability in C9ORF72 ALS/FTD. Brain Res 1693:98–108. https://doi.org/10.1016/J.BRAINRES.2018.02.011
107. Szebényi K, Wenger LMD, Sun Y, Dunn AWE, Limegrover CA, Gibbons GM, Conci E, Paulsen O, Mierau SB, Balmus G, Lakatos A (2021) Human ALS/FTD brain organoid slice cultures display distinct early astrocyte and targetable neuronal pathology. Nat Neurosci 24:1542–1554. https://doi.org/10.1038/s41593-021-00923-4
108. Traag VA, Waltman L, van Eck NJ (2019) From Louvain to Leiden: guaranteeing well-connected communities. Sci Rep 9:1–12. https://doi.org/10.1038/s41598-019-41695-z

109. Umoh ME, Dammer EB, Dai J, Duong DM, Lah JJ, Levey AI, Gearing M, Glass JD, Seyfried NT (2018) A proteomic network approach across the ALS—FTD disease spectrum resolves clinical phenotypes and genetic vulnerability in human brain. EMBO Mol Med 10:48–62. https://doi.org/10.15252/emmm.201708202
110. Uzquiano A, Kedaigle AJ, Pigoni M, Paulsen B, Adiconis X, Kim K, Faits T, Nagaraja S, Antón-Bolaños N, Gerhardinger C, Tucewicz A, Murray E, Jin X, Buenrostro J, Chen F, Velasco S, Regev A, Levin JZ, Arlotta P (2022) Proper acquisition of cell class identity in organoids allows definition of fate specification programs of the human cerebral cortex. Cell 185:3770-3788.e27. https://doi.org/10.1016/j.cell.2022.09.010
111. Vatsavayai SC, Nana AL, Yokoyama JS, Seeley WW (2019) C9orf72-FTD/ALS pathogenesis: evidence from human neuropathological studies. Acta Neuropathol 137:1–26. https://doi.org/10.1007/s00401-018-1921-0
112. Vatsavayai SC, Yoon SJ, Gardner RC, Gendron TF, Vargas JNS, Trujillo A, Pribadi M, Phillips JJ, Gaus SE, Hixson JD, Garcia PA, Rabinovici GD, Coppola G, Geschwind DH, Petrucelli L, Miller BL, Seeley WW (2016) Timing and significance of pathological features in C9orf72 expansion-associated frontotemporal dementia. Brain 139:3202–3216. https://doi.org/10.1093/brain/aww250
113. van Veenhuijzen K, Westeneng HJ, Tan HHG, Nitert AD, van der Burgh HK, Gosselt I, van Es MA, Nijboer TCW, Veldink JH, van den Berg LH (2022) Longitudinal effects of asymptomatic C9orf72 carriership on brain morphology. Ann Neurol. https://doi.org/10.1002/ana.26572
114. Velasco S, Kedaigle AJ, Simmons SK, Nash A, Rocha M, Quadrato G, Paulsen B, Nguyen L, Adiconis X, Regev A, Levin JZ, Arlotta P (2019) Individual brain organoids reproducibly form cell diversity of the human cerebral cortex. Nature 570:523–527. https://doi.org/10.1038/s41586-019-1289-x
115. Verkerke M, Berdenis van Berlekom A, Donega V, Vonk D, Sluijs JA, Butt NF, Kistemaker L, de Witte LD, Pasterkamp RJ, Middeldorp J, Hol EM (2024) Transcriptomic and morphological maturation of human astrocytes in cerebral organoids. Glia 72:362–374. https://doi.org/10.1002/glia.24479
116. Vieira de Sa R, Canizares Luna M, Pasterkamp J (2021) Advances in CNS organoids: a focus on organoid-based models for motor neuron disease. Tissue Eng Part C Methods ten.TEC.2020.0337. https://doi.org/10.1089/ten.TEC.2020.0337
117. Virshup I, Bredikhin D, Heumos L, Palla G, Sturm G, Gayoso A, Kats I, Koutrouli M, Angerer P, Bergen V, Boyeau P, Büttner M, Eraslan G, Fischer D, Frank M, Hong J, Klein M, Lange M, Lopez R, Lotfollahi M, Luecken MD, Ramirez F, Regier J, Rybakov S, Schaar AC, Valiollah Pour Amiri V, Weiler P, Xing G, Berger B, Peer D, Regev A, Teichmann SA, Finotello F, Wolf FA, Yosef N, Stegle O, Theis FJ (2023) The scverse project provides a computational ecosystem for single-cell omics data analysis. Nat Biotechnol 41:604–606. https://doi.org/10.1038/s41587-023-01733-8
118. Virshup I, Rybakov S, Theis FJ, Angerer P, Wolf FA (2021) Anndata: Annotated data. bioRxiv 2021.12.16.473007
119. De Vocht J, Blommaert J, Devrome M, Radwan A, Van Weehaeghe D, De Schaepdryver M, Ceccarini J, Rezaei A, Schramm G, Van Aalst J, Chiò A, Pagani M, Stam D, Van Esch H, Lamaire N, Verhaegen M, Mertens N, Poesen K, Van Den Berg LH, Van Es MA, Vandenberghe R, Vandenbulcke M, Van Den Stock J, Koole M, Dupont P, Van Laere K, Van Damme P (2020) Use of multimodal imaging and clinical biomarkers in presymptomatic carriers of C9orf72 repeat expansion. JAMA Neurol 77:1008–1017. https://doi.org/10.1001/jamaneurol.2020.1087
120. Walhout R, Schmidt R, Westeneng HJ, Verstraete E, Seelen M, Van Rheenen W, De Reus MA, Van Es MA, Hendrikse J, Veldink JH, Van Den Heuvel MP, Van Den Berg LH (2015) Brain morphologic changes in asymptomatic C9orf72 repeat expansion carriers. Neurology 85:1780–1788. https://doi.org/10.1212/WNL.0000000000002135
121. Van Wijk IF, Van Eijk RPA, Van Boxmeer L, Westeneng HJ, Van Es MA, Van Rheenen W, Van Den Berg LH, Eijkemans MJC, Veldink JH (2023) Assessment of risk of ALS conferred by the GGGGCC hexanucleotide repeat expansion in C9orf72 among first-degree relatives of patients with ALS carrying the repeat expansion. Amyotroph Lateral Scler Frontotemporal Degener. https://doi.org/10.1080/21678421.2023.2272187
122. Wolf FA, Angerer P, Theis FJ (2018) SCANPY: large-scale single-cell gene expression data analysis. Genome Biol 19:15. https://doi.org/10.1186/s13059-017-1382-0
123. Xiao S, McKeever PM, Lau A, Robertson J (2019) Synaptic localization of C9orf72 regulates post-synaptic glutamate receptor 1 levels. Acta Neuropathol Commun 7:1–13. https://doi.org/10.1186/s40478-019-0812-5

Publisher's Note